Exact eddy-viscosity equation for turbulent wall flows - Application to CFD models

Emmanuel Plaut[1] & Stefan Heinz[2]
[1]Université de Lorraine, CNRS, LEMTA, F-54000 Nancy, France
[2]Mathematics Department, University of Wyoming, Laramie, WY, USA

Confidential draft **PlautHeinz20.pdf** - Version 0.16 of October 28, 2020

Table of contents

What's new in this Version 0.16 of October 28, 2020/ version 0.15 of October 6, 2020

- The last paragraph of the introduction has been reworked, to advocate the comparison between our ν_t budget and the k budget of section 2.10.
  From there, 'transport' is preferred to 'turbulent diffusion' to name T_ν .
- The titles of the sections 2.3, 2.4 and 2.5 have been shortened.
- The table 1, expanded and reworked, has been moved from section 5 to section 2.10.

- In section 2.10, the property (T1) has been changed.
  A more detailed comparison between our ν_t budget and the k budget is proposed.
  To refer to ϵ profiles I cite Hoyas & Jiménez (2008).
  I created the figures 9 to show production-over-dissipation; thus the former figures 9 to 16 become figures 10 to 17.
- In section 5 I now advocate the log layer and insist on the novelty of our ν_t budgets.

Abstract

A recent theory has been developed (Heinz 2018, 2019) for three canonical turbulent wall flows: channel flow, pipe flow and zero-pressure gradient boundary layer, that offers exact analytical formulas for the RANS eddy-viscosity, as a product of a function of y^+ (the wall-normal distance scaled in inner units) with functions of y/δ (the same distance scaled in outer units). By calculating the eddy-viscosity turbulent diffusion term for these flows where the turbulence is stationary, one identifies a high-Reynolds number eddy-viscosity equation with one production and two dissipation terms. One dissipation term is universal, peaks in the near-wall region, and scales mainly with y^+. The second one, smaller in magnitude, is flow-dependent, peaks in the wake region, and scales mainly with y/δ. The production term is flow-dependent, peaks in between, and scales also mainly with y/δ. The universal dissipation term implies a damping function and a length scale analogous to the von Karman length scale used in the Scale-Adaptive Simulation models of Menter et al. This length scale also appears in the production term. This confirms on firm theoretical bases the relevance of von Karman length scales, and is an occasion to analyze these in more details. An asymptotic analysis of all terms in the eddy-viscosity budget in the limit of infinite Reynolds numbers is also proposed. Asymptotic limit profiles are identified for all terms both in the inner region (y^+ scaling) and in the outer region (y/δ scaling). This allows a review and tests of existing RANS models that imply an eddy-viscosity equation. We thus explain some deficiencies of Spalart & Allmaras (1994); Yoshizawa *et al.* (2012) and propose a modification of the most promising model, i.e., the Scale-Adaptive Simulation model of Menter *et al.* (2006); Menter & Egorov (2010).

---

1 Introduction

Reynolds-Averaged Navier-Stokes (RANS) models are still widely used in Engineering Computational Fluid Dynamics, because they allow studies in complex setups for a lower computational cost than more sophisticated methods like Large Eddy Simulations or Hybrid methods (Wilcox 2006; Hanjalić & Launder 2011). Among RANS models, two-equations models like the $k-\omega$ (Kolmogorov 1942; Wilcox 1988) and $k-\epsilon$ (Launder & Spalding 1974) models are popular. Their equation for the turbulent kinetic energy k is known to be rather accurate. Indeed, its high-Reynolds number form can be validated with direct numerical simulations (DNS - we use those of Lee & Moser 2015) in channel flows, out of the viscous and buffer layers, as shown in the appendix A. On the contrary, the equations for the turbulent dissipation ϵ or the turbulent frequency ω of these models are much less accurate, as shown, with the same DNS data, in the appendix B. These problems are related to the fact that these equations have been constructed empirically on phenomenological and dimensional bases. Alternate RANS models where one turbulent field is the eddy-viscosity ν_t itself, which evolves according to its own equation, look appealing since ν_t is doubtless a quite relevant variable. Whereas the first models of this kind also constructed the ν_t - equation on phenomenological and dimensional bases (Nee & Kovasznay 1969; Baldwin & Barth 1990; Spalart & Allmaras 1994), there have been recently attempts to use more systematic approaches (Yoshizawa *et al.* 2012; Hamba 2013). The Scale-Adaptive Simulation (SAS) models of Menter *et al.* (2006); Menter & Egorov (2010) are also $k-\nu_t$ models, which are more phenomenological than the ones of Yoshizawa *et al.* (2012); Hamba (2013), but may work as Hybrid models. Their ν_t - equation implies, through the so-called von Karman length scale ℓ_{vK} , the second gradient of the mean velocity, which renders them 'sensitive'. In highly non-homogeneous flows the second gradient of the mean velocity, which appears in the denominator of ℓ_{vK} , increases, hence ℓ_{vK} decreases, hence the corresponding dissipation term increases, hence ν_t decreases. This allows resolved motions in unsteady simulations. Relevant applications of variants of this model to quite complex flows are for instance presented in Menter *et al.* (2006); Egorov *et al.* (2010); Abdol-Hamid (2015). Jakirlic & Maduta (2015) also proposed an interesting extension of the SAS approach under the form of a Reynolds stress model.

The facts that many variants of the SAS models exist, and that their equations are built on phenomenological grounds, raise however theoretical questions. Accordingly, it is noticeable that the more systematic approaches of Yoshizawa *et al.* (2012); Hamba (2013) are quite different: whereas Yoshizawa *et al.* (2012) started from a conventional Reynolds stress model, Hamba (2013) started from the nonlocal analysis presented in Hamba (2005). Obviously, there is no perfect way to analytically derive the ν_t - equation.

The aim of this work is to offer a third way, at least for a relevant class of flows: established channel and pipe flows, together with zero-pressure gradient boundary layers over a flat plate. For these three canonical flows, denoted hereafter 'turbulent wall flows', Heinz (2018, 2019) proposed analytic models of the mean flow U, Reynolds shear stress $-\langle u_x u_y \rangle$ and eddy viscosity ν_t , built after a thorough analysis of recent DNS, including those of Lee & Moser (2015); Chin *et al.* (2014); Sillero *et al.* (2013), and experimental data, for instance those of Vallikivi *et al.* (2015). One interest of these models is that they are valid for friction-based Reynolds numbers $Re_\tau \gtrsim 500$: the limit $Re_\tau \to \infty$ is included. Our approach is then to analytically calculate the turbulent diffusion of ν_t and to identify the opposite of this as the sum of a positive production term minus positive dissipation terms, see equation (12). The fact that these terms are analytical offers a much better intellectual understanding of the ν_t - equation, and also a practical understanding of the scaling properties of all terms in this equation. This also permits an accurate description of the limit $Re_\tau \to \infty$. Another goal is the creation of a basis for the numerical and physical evaluation of existing models. This is exemplified on the study of three existing models, and a promising modification of one SAS model is finally derived.

In section 2, we offer a presentation and physical analysis of our model, which considers only high-Reynolds number turbulent wall flows. The physical questions that we want to answer concern the scalings of the production and dissipation terms in the ν_t - equation, and the effects of the flow cases and Reynolds number. Asymptotic formulas valid in the limit $Re_\tau \to \infty$, for all terms in the ν_t - equation, either in the near-wall region (y^+ scaling) or in the outer region (y/δ scaling), are in particular given in the sections 2.6 to 2.9. An overview of all our physical results is offered in the section 2.10, where the differences between the eddy-viscosity budget thus obtained and the known turbulent kinetic energy budget are stressed. The physical results obtained yield a test bench of existing models that imply a ν_t - equation with a standard turbulent diffusion or transport term (T_ν in equation 12). This test bench is used in the section 3 to evaluate three such models: the models of Spalart & Allmaras (1994); Yoshizawa *et al.* (2012) and the SAS models of Menter *et al.* (2006); Menter & Egorov (2010), which have some variants. Finally, the output of these tests is used to propose a modified SAS model in section 4. A concluding section 5 closes this article.

2 Analysis: exact eddy-viscosity formula and transport equation

2.1 Turbulent wall flows - Exact eddy viscosity formula

Following Heinz (2018, 2019), we consider turbulent wall flows of incompressible fluids of mass density ρ and kinematic viscosity ν. Locally, a cartesian system of coordinates Oxyz is used, such that x points in the streamwise direction, and y measures the distance to the closest wall. To lowest order, the mean flow

$$\mathbf{U} \;=\; U(y)\;\mathbf{e}_x \tag{1}$$

with $\mathbf{e}_x$ the unit vector in the x-direction. A relevant quantity is the mean strain rate

$$S \;=\; \partial U/\partial y\;. \tag{2}$$

The macroscopic length scale δ is the half-channel height, pipe radius, or 99% boundary layer thickness with respect to channel flow, pipe flow, and boundary layer, respectively. Denoting $u_x\mathbf{e}_x + u_y\mathbf{e}_y + u_z\mathbf{e}_z$ the fluctuating velocity, the RANS eddy viscosity

$$\nu_t = -\left\langle u_x u_y \right\rangle / S \tag{3}$$

where the angular brackets denote the Reynolds average. The mean wall shear stress τ_w is used to define the friction velocity $u_\tau = \sqrt{\tau_w/\rho}$. From this are defined wall or inner units: $y^+ = u_\tau y/\nu$, $U^+ = U/u_\tau$ and

$$S^+ \;=\; \partial U^+/\partial y^+\;. \tag{4}$$

Finally, the friction-velocity Reynolds number $Re_\tau \;=\; \delta^+ \;=\; u_\tau\delta/\nu$. In the equation (11) of Heinz (2019), an analytic expression is proposed for the reduced eddy viscosity, which is valid at high Reynolds number, $Re_\tau \gtrsim 500$,

$$\nu^+ \;=\; \nu_t/\nu \;=\; (1/S_{12}^+ - 1)\; W\;. \tag{5}$$

There $S_{12}^+ = S_1^+ + S_2^+$ is a very good approximation of the dimensionless mean strain rate S^+ (4) in the inner region of the flows, i.e., disregarding wake effects, see the equation (7) of Heinz (2018) and the corresponding discussion. Precisely, the universal function

$$S_{12}^+ \;=\; S_{12}^+(y^+) \;=\; 1 \;-\; \left[\frac{(y^+/a)^{b/c}}{1+(y^+/a)^{b/c}}\right]^c \;+\; \frac{1}{\kappa y^+}\,\frac{1+h_2/(1+y^+/h_1)}{1+y_k/(y^+H)}\;, \tag{6}$$

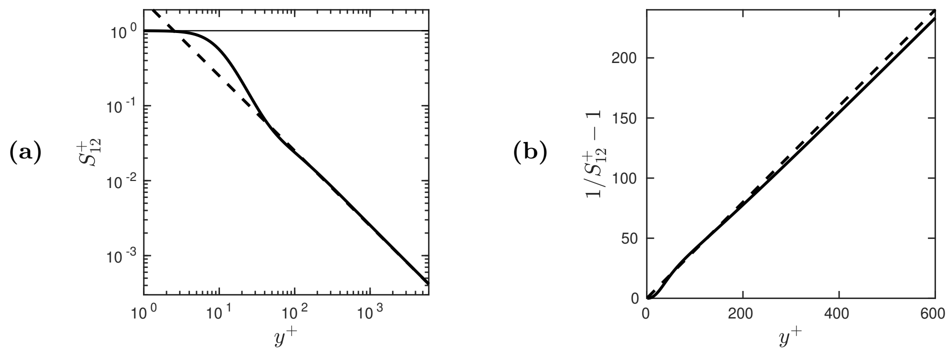

Fig. 1 : **(a)** Continuous curve: S_{12}^+ , dashed line: $1/(\kappa y^+)$. **(b)** Continuous curve: $1/S_{12}^+ - 1$, dashed line: κy^+.

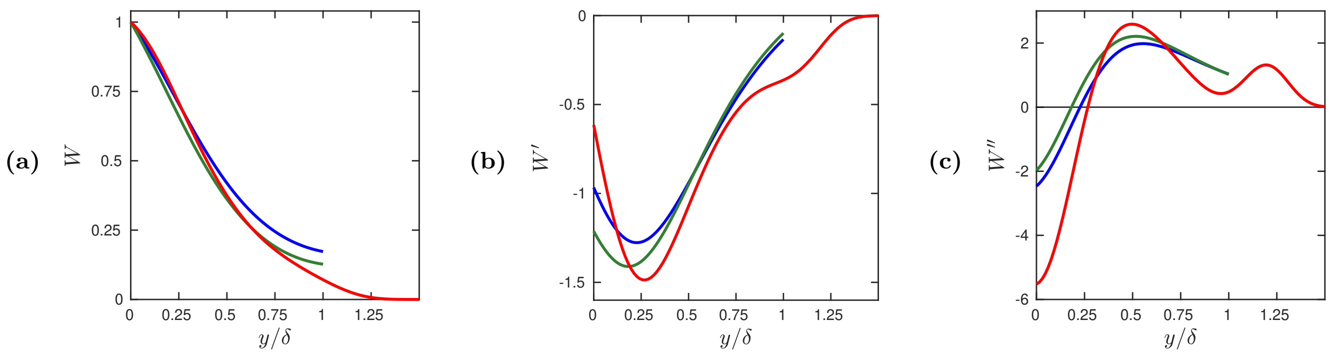

Fig. 2 : **(a)** W **(b)** W' **(c)** W'' for channel (blue), pipe (green), boundary layer (red).

with

$$a = 9, \quad b = 3.04, \quad c = 1.4, \quad H \; = \; H(y^+) \; = \; (1 + h_1/y^+)^{-h_2} \;, \quad h_1 = 12.36, \; h_2 = 6.47, \; y_k = 75.8 \;, \tag{7}$$

and the von Karman constant

$$\kappa \; = \; 0.40 \; . \tag{8}$$

The function S_{12}^+ , plotted on the figure 1a, approaches naturally 1 as $y^+ \to 0$ in the viscous sublayer. On the contrary, as $y^+ \to \infty$, $S_{12}^+ \sim 1/(\kappa y^+)$, in agreement with the log law. Therefore the function $1/S_{12}^+ - 1$, plotted on the figure 1b, which appears in the eddy viscosity (5), vanishes in the limit $y^+ \to 0$, and then increases smoothly to approach the function κy^+ as $y^+ \to \infty$.

The second ingredient of the theory is the function W, which is flow-dependent and in outer scaling, because it describes wake effects. With the notations of Heinz (2018, 2019), $W = 1/G_{CP}$ for channel and pipe flows, M_{BL}/G_{BL} for boundary layers, where G_{CP} and G_{BL} characterize the wake contribution S_3^+ to the dimensionless mean strain rate S^+ (see the equations 7 and A.22 of Heinz 2018), M_{BL} characterizes the total stress in boundary layers (see the equation 4 of Heinz 2019). For channel and pipe flows

$$W \; = \; W_X(y/\delta) \quad \text{with} \quad W_X(y) \; = \; \frac{K_X y + (1-y)^2(0.6y^2 + 1.1y + 1)}{1 + y + y^2(1.6 + 1.8y)} \;, \tag{9}$$

$X = C,\; K_C = 0.933$ for channel, $X = P,\; K_P = 0.687$ for pipe; for boundary layers

$$W \; = \; W_{BL}(y/\delta) \quad \text{with} \quad W_{BL}(y) \; = \; \frac{1 + 0.285 \; y \; e^{y(0.9+y+1.09y^2)}}{1 + (0.9 + 2y + 3.27y^2)y} \;\; e^{-y^6 - 1.57y^2} \;. \tag{10}$$

The wake function W is plotted for these three flows on the figure 2a. In the near-wall region, when $y/\delta \to 0$, $W \to 1$, hence the eddy viscosity (5), $\nu^+ \; = \; (1/S_{12}^+(y^+) - 1) \; W(y^+/\delta^+) \; \sim \; (1/S_{12}^+(y^+) - 1)$. Therefore the log-layer eddy viscosity κy^+ is approximately recovered if $1 \ll y^+ \ll \delta^+$; for a more precise discussion, see the section 4.1 of Heinz (2019). When y becomes of the order of δ, wake effects come in, that saturate the growth of the eddy viscosity (5), since W decreases. The maximum value of y is δ in channel and pipe flows: if $y \in [\delta, 2\delta]$ the mean fields can be obtained by suitable symmetries from the mean fields for $y \in [0, \delta]$. On the contrary, y may be much larger in boundary layers. Naturally, $W_{BL} \to 0$ as $y \to \infty$; precisely $W_{BL} < 10^{-3}$ as soon as $y > 1.36\delta$.

This model has been validated by a study of DNS and experimental data. For instance, the figures S.6abc of the supplementary material to Heinz (2019) show the eddy viscosity of various DNS, one for each canonical flow, compared

with two variants of the eddy-viscosity model (5). In particular, the magenta curves show $\nu^+ = \kappa y^+ \, W$ with our notations, i.e. $(1/S_{12}^+ - 1)$ in (5) has been replaced by κy^+. The agreement with the DNS is good, except in the outer region, where in (3) both the numerator $\langle u_x u_y \rangle$ and the denominator S tend to zero, hence the DNS noise is amplified. A direct comparison between the model (5) and channel flow DNS is displayed on our figures 15bc.
Since the derivatives W' and W'' will be needed hereafer, they are plotted on the figures 2bc. Whereas the functions W for the three flow cases are similar (figure 2a), their first and second derivatives show larger differences (figures 2bc). Naturally, W'_{BL} and $W''_{BL} \to 0$ as $y \to \infty$.

2.2 Exact eddy-viscosity equation for turbulent wall flows

Since the focus of our study is on high-Reynolds numbers wall-bounded flows, we assume that the eddy-viscosity equation takes the standard form

$$\sigma \frac{\partial \nu_t}{\partial t} \;=\; \frac{\partial}{\partial y}\Big(\nu_t \frac{\partial \nu_t}{\partial y}\Big) \;+\; P_\nu \;-\; D_\nu \tag{11}$$

with $P_\nu > 0$ the production, $D_\nu > 0$ the dissipation term. The dimensionless coefficient σ, of order 1, which is a 'turbulent Prandtl number', plays no role in the turbulent wall flows, where the mean fields are steady, but is kept in (11) for the sake of comparison with existing turbulence models. In turbulent wall flows, according to (11), the opposite of the turbulent diffusion term, or transport term,

$$-\,T_\nu \;=\; -\,\frac{\partial}{\partial y}\Big(\nu_t \frac{\partial \nu_t}{\partial y}\Big) \;=\; P_\nu \;-\; D_\nu \;. \tag{12}$$

A calculation of T_ν starting from (5) leads to $D_\nu \;=\; D_{\nu i} \;+\; D_{\nu o}$ and

$$D_{\nu i} \;=\; \kappa^2 \,\frac{\nu_t^2}{L_{vK}^2}\, \frac{1}{f^2} \;, \tag{13a}$$

$$P_\nu \;=\; \kappa \,\frac{\nu_t^2}{L_{vK}\;\delta}\, \frac{1}{1 - S_{12}^+} \,\Big(-\frac{4W'}{W}\Big) \;=\; \kappa \,\frac{\nu\;\nu_t}{L_{vK}\;\delta}\, \frac{1}{S_{12}^+}\,(-4W')\;, \tag{13b}$$

$$D_{\nu o} \;=\; \frac{\nu_t^2}{\delta^2}\, \frac{W'^2 + WW''}{W^2} \;=\; \frac{\nu^2}{\delta^2}\,(1/S_{12}^+ - 1)^2\,(W'^2 + WW'')\;. \tag{13c}$$

The indices i and o refer to 'inner' and 'outer' terms, respectively, and the notation $D_{\nu o}$ is slightly improper since this term is slightly negative in the near-wall region. However, $D_{\nu o}$ is much smaller in this region than in the outer region where it peaks, as it will be shown in the figure 6b for channel flow, 7b for pipe flow, 8b for boundary layers. Moreover $D_\nu \;=\; D_{\nu i} \;+\; D_{\nu o} > 0$ everywhere, as it will be shown in the figures 6cd for channel flow, 7cd for pipe flow, 8cd for boundary layers, hence the notation D_ν is fully justified.
In addition to the functions S_{12}^+ and W defined in the section 2.1, there appears in the equations (13) other functions that are built on these. The first one is the asymptotic von Karman length scale

$$L_{vK} \;=\; \kappa \,\Big|\frac{S_{12}}{\partial S_{12}/\partial y}\Big| \quad \text{or} \quad L_{vK}^+ \;=\; \kappa \,\Big|\frac{S_{12}^+}{\partial S_{12}^+/\partial y^+}\Big|\;. \tag{14}$$

It is defined as the von Karman length scale used by the SAS models

$$\ell_{vK} \;=\; \kappa \,\Big|\frac{S}{\partial S/\partial y}\Big|\;, \tag{15}$$

but replacing S by S_{12} , i.e., disregarding 'wake effects'. The fact that the length scale L_{vK} appears in (13a) and (13b) confirms on very firm bases the relevance of this length scale, which was not so clear in the derivation of Menter *et al.* (2006); Menter & Egorov (2010). Only the inner-units $L_{vK}^+(y^+)$ is universal, whereas in outer units $L_{vK}(y)/\delta$ has to be calculated as L_{vK}^+/δ^+ at $y^+ = \delta^+(y/\delta)$: it depends on $\delta^+ = Re_\tau$. Since, as $y^+ \to \infty$, in agreement with the log law, $S_{12}^+ \sim 1/(\kappa y^+)$, $L_{vK}^+ \sim \kappa y^+$, as confirmed by the figure 3a. The functions $\ell_{vK}^+(y^+)$ (figure 3a) or $\ell_{vK}(y/\delta)$ (figure 3b), that depend on the flow case and Reynolds-number, have been computed using the accurate expressions of S^+ of the equation (7) of Heinz (2018), that take into account wake effects. In channel or pipe flow, U presents a maximum at the centerplane or pipe axis $y = \delta$, hence S and ℓ_{vK} vanish there. On the contrary, in boundary layer flow, S and ℓ_{vK} vanish only in the limit $y \to \infty$. Phenomenologically, L_{vK} and ℓ_{vK} become large in the viscous sublayer, because there the velocity profile becomes linear ($U \propto y$), then they diminish in the buffer layer where there are strong gradients; further away in the outer region L_{vK} and ℓ_{vK} again become large because the velocity profile flattens. The wake effects finally saturate the growth of ℓ_{vK} and even impose a decrease of ℓ_{vK} , as already explained, but do not influence L_{vK} . The figure 3c suggests that, because the dimensional factor in $D_{\nu i}$ (13a), P_ν

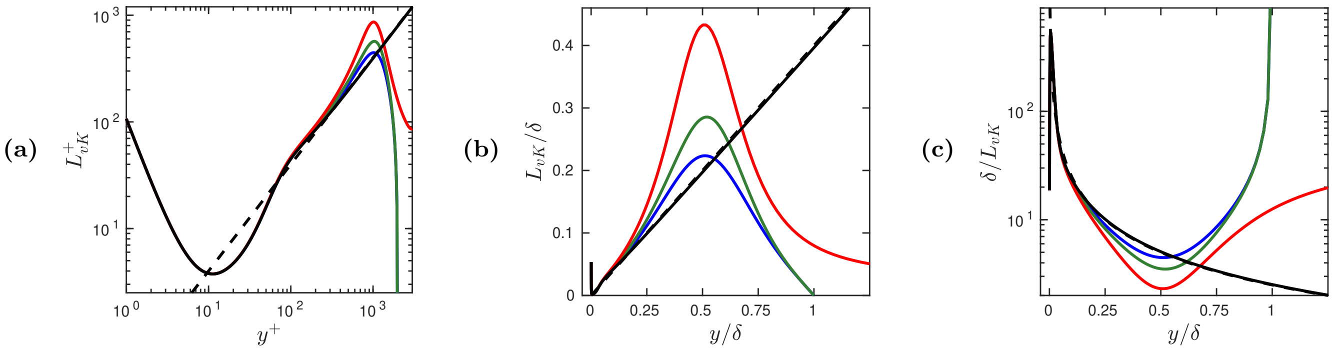

Fig. 3 : **(a,b)** The asymptotic von Karman length scale L_{vK} (14) (black continuous); its log law approximation κy (black dashed); the von Karman length scale ℓ_{vK} (15) for channel (blue), pipe (green), boundary layer (red). The ℓ^+_{vK} curves of the figure **(a)** and all curves of the figure **(b)** have been computed at $Re_\tau = 1995$. The figure **(c)** shows the same curves as figure **(b)** but with the inverse ordinates and linear-log scales. All curves in **(a,b,c)** start at $y^+ = 1$.

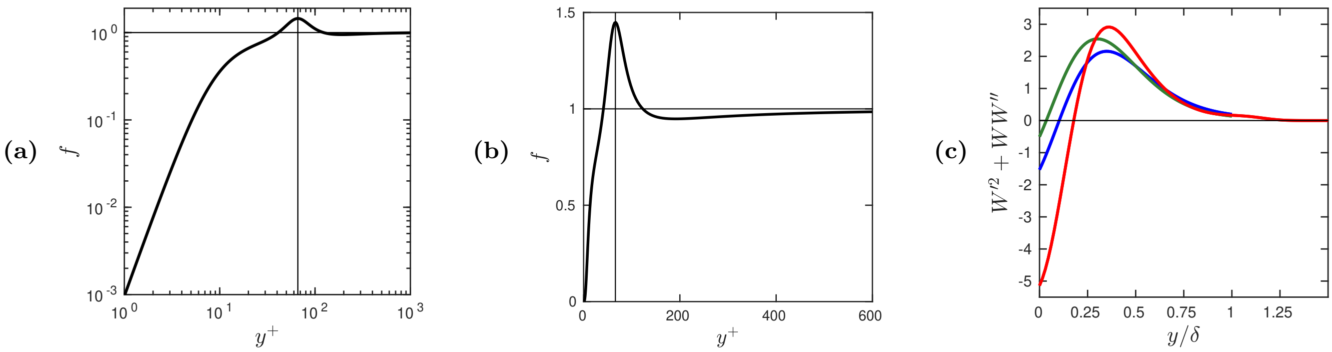

Fig. 4 : **(a,b)** The damping function f. The vertical lines are at $y^+ = 66$. **(c)** The function $W'^2 + WW''$ for channel (blue), pipe (green), boundary layer (red).

(first expression in 13b) and $D_{\nu o}$ (first expression in 13c) are respectively ν_t^2/L^2_{vK} , $\nu_t^2/(L_{vK}\delta)$ and ν_t^2/δ^2, in the ratii δ^2/L^2_{vK} , δ/L_{vK} , 1, those will peak in the inner, intermediate and outer regions. This will be confirmed in the figures 6 for channel flow, 7 for pipe flow, 8 for boundary layers.
Another ingredient in $D_{\nu i}$ (13a) is the universal damping function

$$f \;=\; f(y^+) \;=\; (1 - S^+_{12})\left(\frac{(S^+_{12} - 1)\; S^+_{12}\; d^2 S^+_{12}/dy^{+2}}{(dS^+_{12}/dy^+)^2} + 3 - 2S^+_{12}\right)^{-1/2} . \tag{16}$$

It is plotted on the figures 4ab. It does tend to zero as $y^+ \to 0$ and 1 as $y^+ \to \infty$.
Finally, in P_ν (13b) and $D_{\nu o}$ (13c) the rightmost functions depend only on W and its derivatives. In P_ν there appears $-4W'$ which is positive according to the figure 2b, hence $P_\nu > 0$ as required. In $D_{\nu o}$ there appears $W'^2 + WW''$ which is plotted on the figure 4c. The function $W'^2 + WW'' > 0$ except in a more or less narrow near-wall region, depending on the flow case: this impacts the sign of $D_{\nu o}$ as already discussed after the equations (13).

2.3 The channel flow case

In typical channel flow cases, a comparison of the opposite of the dimensionless transport term

$$-\,T^+_\nu \;=\; -\,\frac{\partial}{\partial y^+}\left(\nu^+\frac{\partial \nu^+}{\partial y^+}\right) \;=\; -\,\frac{T_\nu}{u^2_\tau} \tag{17}$$

computed with finite differences from two DNS of Lee & Moser (2015) and its model (12,13),

$$-\,T^+_\nu \;=\; P^+_\nu \;-\; D^+_\nu \;=\; -\;D^+_{\nu i} \;+\; P^+_\nu \;-\; D^+_{\nu o} \tag{18}$$

is shown on the figures 5. Except in the outer region, where the DNS noise is amplified, there is a good agreement between the model and the DNS, especially for the highest Reynolds number case.
The separation of $-T^+_\nu$ into the three terms of the model, $-D^+_{\nu i}$, P^+_ν and $-D^+_{\nu o}$, is illustrated on the figures 6. The figures 6a, c and g shows that the dissipation term $D^+_{\nu i}$ dominates in the near-wall region. In this region, and in inner

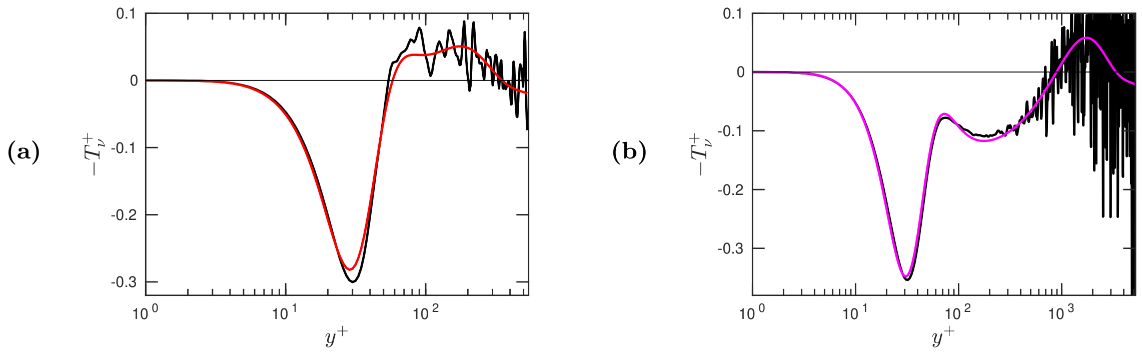

Fig. 5 : The black curve shows the opposite of the dimensionless transport term $-T_\nu^+$ (17) computed with the channel flow DNS of Lee & Moser (2015) at $Re_\tau = 543$ **(a)**, 5186 **(b)**. The colored curves show the same term computed with our model (18).

scalings, $D_{\nu i}^+(y^+)$, $D_\nu^+(y^+)$ and $T_\nu^+(y^+)$ approach as $Re_\tau \to \infty$ a limit profile $-D_{\nu ia}^+$, which is plotted in black, and will be studied in the section 2.6. A plateau around $y^+ \simeq 400$ and

$$D_{\nu i}^+ \;\simeq\; D_\nu^+ \;\simeq\; T_\nu^+ \;\simeq\; \kappa^2$$

builds up as $Re_\tau \to \infty$, in agreement with the formula for the log-layer reduced eddy viscosity, $\nu^+ = \kappa y^+$. For larger values of y/δ, after this plateau, the figures 6bdfh show that all terms, considered in inner-outer scalings, $D_{\nu i}^+(y/\delta)$, $D_{\nu o}^+(y/\delta)$, $D_\nu^+(y/\delta)$, $P_\nu^+(y/\delta)$ and $T_\nu^+(y/\delta)$, approach limit profiles as $Re_\tau \to \infty$. These limit profiles, plotted in black for the three latest functions, denoted $-D_{\nu a}^+$, $P_{\nu a}^+$ and $-T_{\nu a}^+$, will be studied in the sections 2.7, 2.8 and 2.9.

2.4 The pipe flow case

In the eddy-viscosity formula (5), the only difference between channel and pipe flows is described by the change of the coefficient K_X in the function W_X (9) that contains the wake effects. This change from $K_C = 0.933$ to $K_P = 0.687$ is moderate, therefore the transport term and its contributions are close to the ones of channel flow, as shows the comparison between the figures 6 and figures 7. All the comments made on the figures 6 at the end of section 2.3 also apply to the figures 7.

2.5 The boundary layer case

The boundary layer case differs from the channel and pipe flow cases in that the maximum value of y (resp. y^+) is not δ (resp. $\delta^+ = Re_\tau$) but, in principle, infinity. Moreover, the wake function W_{BL} of boundary layers (10) differs significantly from the one of channel and pipe flows (9). The comparison of the figures 8 with the figures 6 and 7 shows similar behaviours in the ranges $y \in [0, \delta[$ i.e. $y^+ \in [0, \delta^+[$, whereas there are differences in the outer region. At $y = \delta$, i.e. the centerplane in channels or the pipe axis in pipes, the function T_ν should present a vanishing slope for symmetry reasons, as confirmed by the figures 6h and 7h; note that the outer term $-D_{\nu o}^+$ plays an important role there. In boundary layers, one does not expect a similar property, but that T_ν should approach 0 as $y \to \infty$. This is what suggests the figure 8h, and what would confirm a figure drawn with a larger interval of the abscissas: for all the Reynolds numbers implied, that range from 543 to 80000, $|T_\nu^+| < 10^{-3}$ as soon as $y > 1.32\delta$.

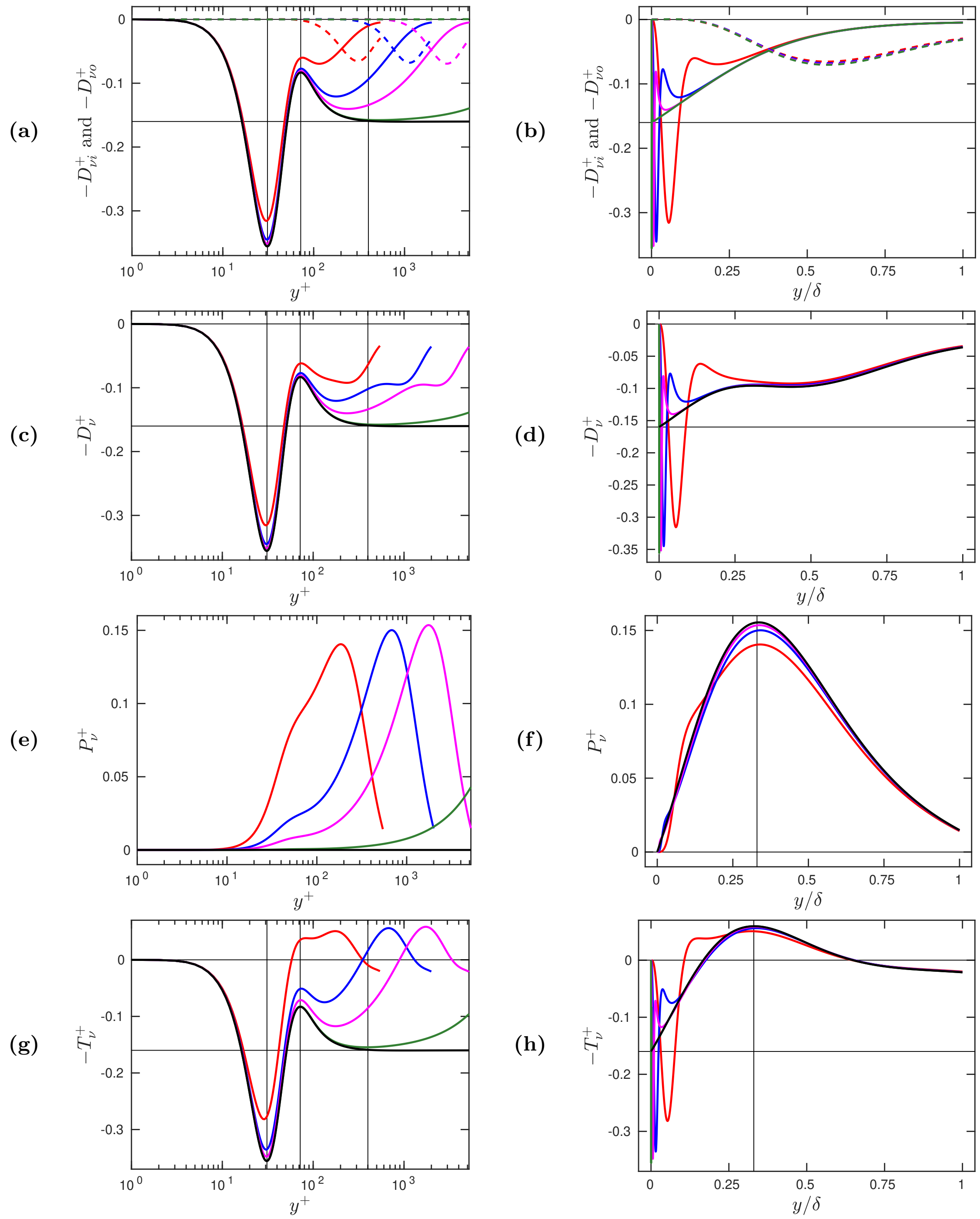

Fig. 6 : For channel flows, the colored curves, at $Re_\tau = 543$ (red), 1995 (blue), 5186 (magenta), 80000 (green), show the various contributions to $-T^+_\nu$ (18) and their sum. **(a,b)** $-D^+_{\nu i}$ (resp. $-D^+_{\nu o}$): continuous (resp. dashed) curves. **(c,d)** $-D^+_\nu$. **(e,f)** P^+_ν . **(g,h)** $-T^+_\nu$. The black curves show the asymptotic profiles approached as $Re_\tau \to \infty$ either at fixed y^+ in **(a,c,g)** or fixed y/δ in **(d,f,h)**. **(a,c,g)** $-D^+_{\nu ia}$. **(d)** $-D^+_{\nu a}$. **(f)** $P^+_{\nu a}$. **(h)** $-T^+_{\nu a}$. On **(a,c,g)** the vertical lines are at $y^+ = 31$, 72 and 400; on **(f,h)** they are at $y = 0.33\delta$. On **(a,b,c,d,g,h)** the horizontal lines are at $-T^+_\nu = 0$ and $-\kappa^2$.

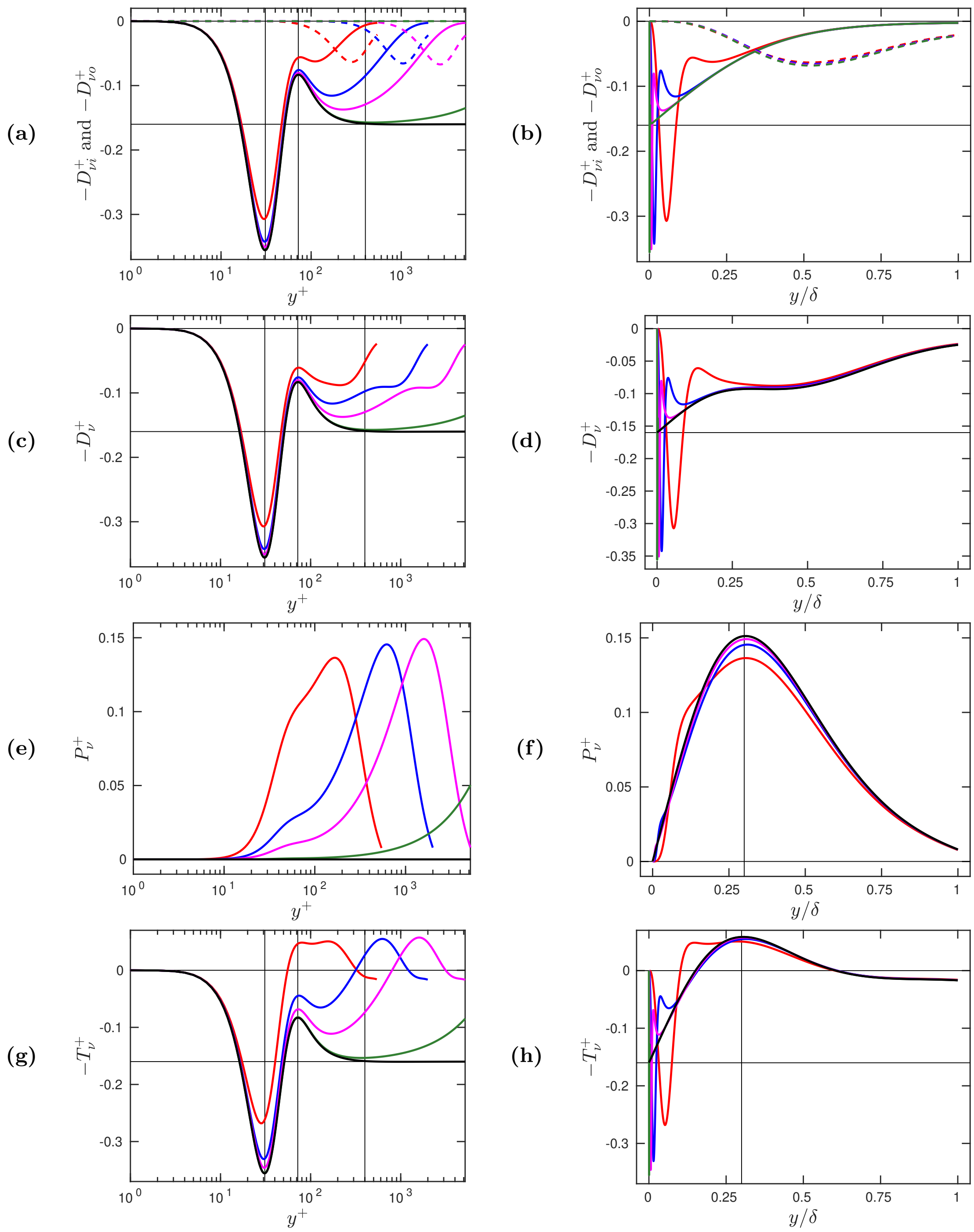

Fig. 7 : Same as figure 6, but for pipe flows. On **(f,h)** the vertical lines are at $y = 0.3\delta$.

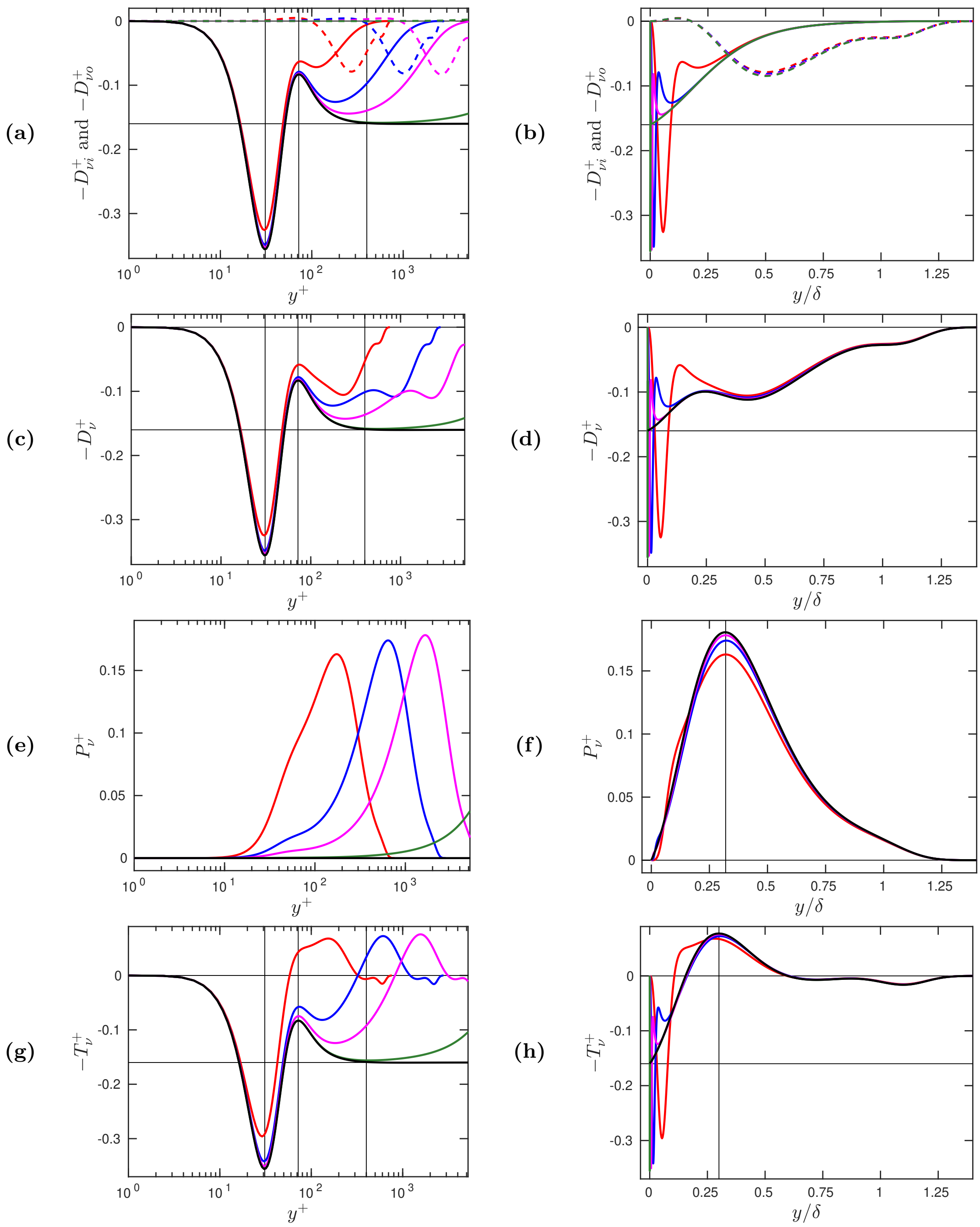

Fig. 8 : Same as figure 6, but for boundary layers. On **(f)** the vertical line is at $y = 0.32\delta$, on **(h)** it is at $y = 0.3\delta$.

2.6 Universal asymptotic profile of the dissipation in the inner region

The figures 6aceg, 7aceg and 8aceg show that, as $Re_\tau \to \infty$, the dissipation term $D_{\nu i}$ dominates the eddy-viscosity budget in the inner region, that it scales with y^+, and approaches in inner units a universal asymptotic profile. This profile is obtained by replacing, in the expression (5) of the eddy-viscosity, which appears at the power 2 in $D_{\nu i}$ (13a), the wake function W by 1, since then the wake region goes to infinity in inner scaling: at fixed y^+, $y/\delta = y^+/Re_\tau \to 0$ as $Re_\tau \to \infty$. This yields the asymptotic dissipation function

$$D_{\nu ia} \;=\; \kappa^2 \,\frac{\nu^2}{L_{vK}^2}\, \frac{(1/S_{12}^+ - 1)^2}{f^2} \qquad \text{or} \qquad D_{\nu ia}^+ \;=\; \kappa^2 \,\frac{(1/S_{12}^+ - 1)^2}{L_{vK}^{+2}}\, \frac{1}{f^2}\;. \tag{19}$$

It is universal in that it does not depend on the flow case, but only on S_{12}^+ , see the equations (14) and (16). Moreover, $D_{\nu ia}^+$ considered as a function of y^+ also does not depend on Re_τ . The function $-D_{\nu ia}^+$ is plotted in black on the figures 6acg, 7acg and 8acg. It is approached at fixed y^+, when $Re_\tau \to \infty$, by $-D_{\nu i}^+$, $-D_\nu^+$ and $-T_\nu^+$. On the figures 6acg, 7acg and 8acg, the first vertical line at $y^+ = 31$ indicates the dissipation peak, with max $D_{\nu ia}^+ \simeq 0.36$, the second vertical line at $y^+ = 72$ indicates a local minimum of dissipation, whereas the third vertical line at $y^+ = 400$ indicates the log-layer plateau. Indeed, as $y^+ \to \infty$, since $1/S_{12}^+ - 1$ and L_{vK}^+ approach κy^+, whereas $f \to 1$, one has $D_{\nu ia}^+ \to \kappa^2$, in agreement with the expression of the log-layer eddy viscosity $\nu^+ = \kappa y^+$. Precisely, $|D_{\nu ia}^+ - \kappa^2| < 10^{-3}$ as soon as $y^+ \geq 400$. From a physical point of view, these results prove that near-wall dissipation is due to universal near-wall motions.

2.7 Asymptotic profile of the production in the outer region

The figures 6ef, 7ef and 8ef show that, as $Re_\tau \to \infty$, the production of the eddy viscosity vanishes in the inner region, scales with y/δ, and approaches in the outer region asymptotic profiles that depend only on the flow case. These profiles are obtained by replacing, in the second expression of P_ν (13b), transformed in inner units,

$$P_\nu^+ \;=\; \kappa\,\frac{\nu^+}{S_{12}^+\, L_{vK}^+\, \delta^+}\,(-4W')\;, \tag{20}$$

the eddy viscosity ν^+, the strain rate S_{12}^+ and the von Karman length-scale L_{vK}^+ by their approximations valid as $y^+ \to \infty$, i.e. $\kappa y^+\, W$, $1/\kappa y^+$ and κy^+ respectively, see the discussions after equations (5-8) for ν^+ and S_{12}^+ , equations (14-15) for L_{vK}^+ . This yields the asymptotic profiles

$$P_{\nu a}^+ \;=\; \kappa^2\,\frac{y}{\delta}\,(-4WW') \qquad \text{or} \qquad P_{\nu a} \;=\; \kappa^2\, u_\tau^2\,\frac{y}{\delta}\,(-4WW')\;. \tag{21}$$

The first equation shows that $P_{\nu a}^+$ is, for a fixed flow case, a function of y/δ only, because the wake function W depends only on y/δ, see equations (9-10). The functions $P_{\nu a}^+$ are plotted in black on the figure 6f for channel flow, 7f for pipe flow, 8f for boundary layer. These figures confirm that, at fixed y/δ, P_ν^+ approaches $P_{\nu a}^+$ as $Re_\tau \to \infty$. From a physical point of view, these results prove that production is due to large-scale outer motions. The comparison between the vertical scales of the figures 6f, 7f and 8f shows that these motions contribute more efficiently to the production of ν_t in the boundary layer than in the other flows. This is probably related to the fact that the boundary layer is in principle unbounded in the wall-normal direction, contrarily to channel and pipe flows.

2.8 Asymptotic profile of the dissipation in the outer region

The figures 6bd, 7bd and 8bd show that, as $Re_\tau \to \infty$, in the outer region, the dissipation terms $D_{\nu i}^+$, $D_{\nu o}^+$ and their sum D_ν^+ scale with y/δ, and approach asymptotic profiles that depend only on the flow case. These profiles are obtained by starting from the expressions (13a) and (13c), transformed in inner units,

$$D_\nu^+ \;=\; \kappa^2\,\frac{\nu^{+2}}{L_{vK}^{+2}}\,\frac{1}{f^2} \;+\; \frac{1}{\delta^{+2}}\,(1/S_{12}^+ - 1)^2\,(W'^2 + WW'')\;, \tag{22}$$

and applying the approximations that led from (20) to (21), plus $f \simeq 1$. This yields the asymptotic profiles

$$D_{\nu a}^+ \;=\; \kappa^2\, W^2 \;+\; \kappa^2 \left(\frac{y}{\delta}\right)^2 (W'^2 + WW'') \qquad \text{or} \qquad D_{\nu a} \;=\; \kappa^2\, u_\tau^2\, W^2 \;+\; \kappa^2\, u_\tau^2 \left(\frac{y}{\delta}\right)^2 (W'^2 + WW'')\;, \tag{23}$$

where the first (resp. second) terms correspond to the asymptotic profile of $D_{\nu i}^+$ or $D_{\nu i}$ (resp. $D_{\nu o}^+$ or $D_{\nu o}$). Similar to $P_{\nu a}^+$ (21), $D_{\nu a}^+$ is, for a fixed flow case, a function of y/δ only. The functions $-D_{\nu a}^+$ are plotted in black on the figure 6d for channel flow, 7d for pipe flow, 8d for boundary layer. They are well approached by $-D_\nu^+$ as $Re_\tau \to \infty$.

	Transport	Production	Dissipation
Finite Re_τ	T_ν	P_ν eq. (13b)	$D_\nu \ = \ D_{\nu i} + D_{\nu o}$ eq. (13a,13c)
Infinite Re_τ - inner region	$D_{\nu ia}(y^+)$ eq. (19)	0	$D_{\nu ia}(y^+)$ eq. (19)
Infinite Re_τ - log layer	$u_\tau^2 \kappa^2$	0	$u_\tau^2 \kappa^2$
Infinite Re_τ - outer region	$T_{\nu a}(y/\delta)$ eq. (24)	$P_{\nu a}(y/\delta)$ eq. (21)	$D_{\nu a}(y/\delta)$ eq. (23)

Tab. 1 : The different terms in the ν_t - equation, or ν_t - budget, $0 = T_\nu + P_\nu - D_\nu$, at finite and infinite Re_τ , in various regions for this latter case, with analytical formulas or references to analytical formulas.

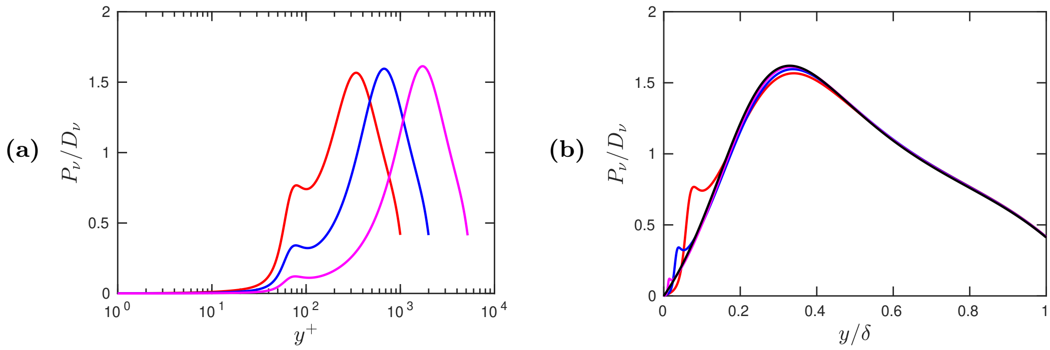

Fig. 9 : Production to dissipation ratio in channel flow, for $Re_\tau = 1000$ (red), 1995 (blue), 5186 (magenta). In **(b)** the black curve shows the asymptotic ratio $P_{\nu a}/D_{\nu a}$.

2.9 Asymptotic profile of the transport term in the outer region

Obviously

$$-\,T^+_{\nu a} \ = \ P^+_{\nu a} \ - \ D^+_{\nu a} \quad \text{or} \quad -\,T_{\nu a} \ = \ P_{\nu a} \ - \ D_{\nu a} \ , \tag{24}$$

depending on the units, yields the asymptotic profiles of the opposite of the transport term in the outer region, as proven by the figures 6h for channel flow, 7h for pipe flow, 8h for boundary layer.

2.10 Overview of the physical properties of the exact ν_t - equation

From the results of the sections 2.2 to 2.9, we can construct for an overview the table 1, and list the following physical properties of the exact ν_t - equation.

(D0) The dissipation term $-D_{\nu i}$, that mainly scales with y^+, dominates all the other terms in the inner region.

(D1) As $Re_\tau \to \infty$, $D^+_{\nu i}$ converges to a universal function $D^+_{\nu ia}(y^+)$ that peaks at $\max D^+_{\nu ia} \simeq 0.36$ around $y^+ = 31$.

(D2) For larger values of y^+, $D^+_{\nu ia}$ has a minimum around $y^+ = 72$, and reaches the log-layer plateau $D^+_{\nu ia} \ = \ \kappa^2$ as soon as $y^+ \gtrsim 400$.
All this proves that dissipation of the eddy-viscosity is mainly due to universal near-wall motions.

(T0) Beyond the log-layer plateau in terms of values of y, and as $Re_\tau \to \infty$, the opposite of the transport term $-T^+_\nu$ converges to asymptotic profiles $-T^+_{\nu a}$ that depend on y/δ and on the flow case only. These asymptotic profiles start at 'low' y at the log-layer plateau value $-T^+_{\nu a} \ = -\kappa^2$.

(P) For larger values of y, the functions $-T^+_{\nu a}$ show a maximum due to the production term around $y = 0.3\delta$.
The scaling with y/δ and the position of this maximum proves that production of the eddy-viscosity is due to large-scale outer motions.

(T1) For even larger values $y \geq 0.65\delta$, $\ -0.025 < -T^+_{\nu a} < 0$, i.e. dissipation dominates again, but only slightly.

The properties (D) contrast with the ones of the dissipation of the turbulent kinetic energy k, i.e., ϵ, which peaks at the wall and shows no clear scaling, as shown for instance in Hoyas & Jiménez (2008). The properties (P) contrast strongly with the ones of the production of k, which scales with y^+ and peaks around $y^+ = 11$, as shown for instance in the supplementary material to Heinz (2019). To further illustrate these differences between the eddy-viscosity and turbulent kinetic energy budgets, the production to dissipation ratio is shown on the figures 9. The comparison of the figure 9a with the figure 7 of Lee & Moser (2015) that displays $P_k/\epsilon - 1$ (with their notations, see also our appendix A) shows huge differences: when $Re_\tau \to \infty$, whereas at fixed y^+ one has $P_\nu \to 0$, on the contrary P^+_k and ϵ^+ seem to

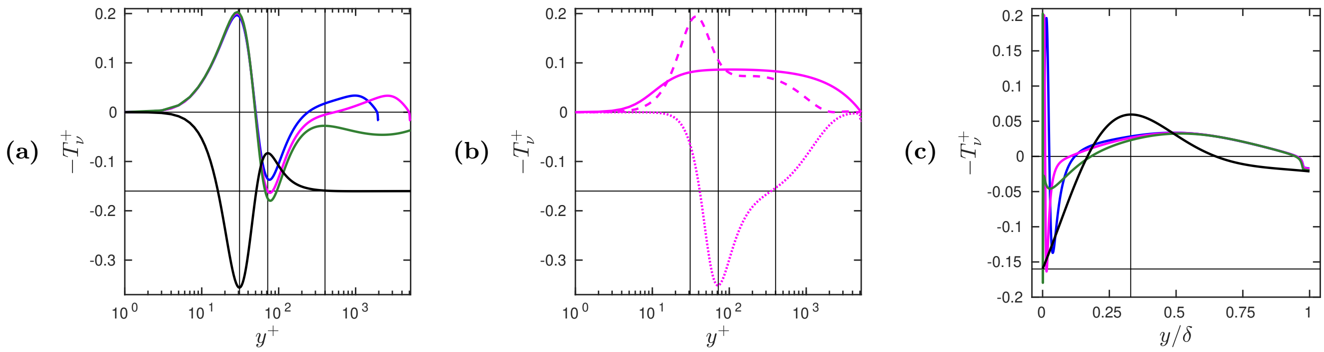

Fig. 10 : Evaluation of the model of Spalart & Allmaras (1994) in channel flow. In **(a)**, the black curve shows $-D^+_{\nu ia}$ (19), the colored curves show $-T^+_{\nu S}$ (27) for Re_τ = 1995 (blue), 5186 (magenta) and 80000 (green). In **(b)**, for Re_τ = 5186, the curves show $\sigma_S c_{b1} S^+ \nu^+$ (continuous), $c_{b2}\ (\partial\nu^+/\partial y^+)^2$ (dashed), $-\sigma_S c_{w1}\ f_w\ (\nu^+/y^+)^2$ (dotted). In **(a,b)** the vertical lines are at $y^+ = 31,\ 72$ and 400. In **(c)**, the black curve shows $-T^+_{\nu a}$ (24), the colored curves show $-T^+_{\nu S}$ for Re_τ = 1995 (blue), 5186 (magenta) and 80000 (green), the vertical line is at $y = 0.33\delta$. In **(a,b,c)** the horizontal lines are at $-T^+_\nu = 0$ and $-\kappa^2$.

converge to finite values. Moreover, whereas $P_k = 0$ at the centerplane in channel flow for symmetry reasons, $P_\nu > 0$ there. The figure 9b shows at fixed y/δ the convergence of P_ν/D_ν to the asymptotic profile $P_{\nu a}/D_{\nu a}$. Overall, the eddy-viscosity and turbulent kinetic energy budgets differ significantly.
The robust properties (D,T,P) will now be used to study existing models of the eddy-viscosity equation.

3 Evaluation of other eddy-viscosity models

From now on, the focus is on channel flows, which are very well documented, and where the geometry is the most simple. Our aim is a review of existing models of the eddy-viscosity equation, by a test of the properties listed in the section 2.10 through relevant plots.

3.1 About the model of Spalart & Allmaras (1994)

The high-Reynolds number eddy-viscosity equation (4) of Spalart & Allmaras (1994) reads, for channel flow,

$$\sigma_S \frac{\partial \nu_t}{\partial t} \;=\; 0 \;=\; \frac{\partial}{\partial y}\left(\nu_t \frac{\partial \nu_t}{\partial y}\right) \;+\; c_{b2}\left(\frac{\partial \nu_t}{\partial y}\right)^2 \;+\; \sigma_S c_{b1} S \nu_t \;-\; \sigma_S c_{w1}\ f_w\ \left(\frac{\nu_t}{y}\right)^2 , \tag{25}$$

with the same notations, except for σ_S which stands for the σ of Spalart & Allmaras (1994), and

$$f_w \;=\; g\ \left(\frac{1+c_{w3}^6}{g^6+c_{w3}^6}\right)^{1/6} ,\quad g \;=\; r + c_{w2}(r^6 - r) ,\quad r \;=\; \frac{\nu_t}{S\ \kappa_S^2\ y^2} , \tag{26}$$

$\sigma_S = 2/3,\ c_{b1} = 0.1355,\ c_{b2} = 0.622,\ \kappa_S = 0.41,\ c_{w1} = c_{b1}/\kappa_S + (1+c_{b2})/\sigma_S = 2.763,\ c_{w2} = 0.3,\ c_{w3} = 2$; their von Karman constant κ_S differs slightly from ours (8). With the definitions (12) and (17) of the transport term in physical and dimensionless forms, we identify their model for $-T^+_\nu$,

$$-\,T^+_{\nu S} \;=\; \sigma_S c_{b1} S^+ \nu^+ \;+\; c_{b2}\left(\frac{\partial \nu^+}{\partial y^+}\right)^2 \;-\; \sigma_S c_{w1}\ f_w\ \left(\frac{\nu^+}{y^+}\right)^2 \tag{27}$$

with, in particular,

$$r \;=\; \frac{\nu^+}{S^+\ \kappa_S^2\ y^{+2}} . \tag{28}$$

To compute S^+ accurately, for the evaluation of the first and third terms in (27), the equation (7) of Heinz (2018), that takes into account wake effects, is used. The model (5) is used on the other hand to compute ν^+. As a first test of Spalart & Allmaras (1994) model, plots in the inner region, with y^+ as the abscissa, are displayed on the figures 10ab. According to the properties (D0,D1) of the exact ν_t − equation, the colored curves of the figure 10a should approach, at fixed y^+, as Re_τ increases, the black curve showing $-D^+_{\nu ia}$. This is not the case, and more seriously the model of Spalart & Allmaras (1994) predicts a near-wall production peak where there should be a near-wall dissipation peak. The figure 10b confirms that the dissipation peak of the model occurs at too large values of y^+, and also shows that the inclusion of the differential production term proportional to $(\partial\nu^+/\partial y^+)^2$ does not help: it adds production where there should be more dissipation. Thus the high-Reynolds number model of Spalart & Allmaras (1994) does

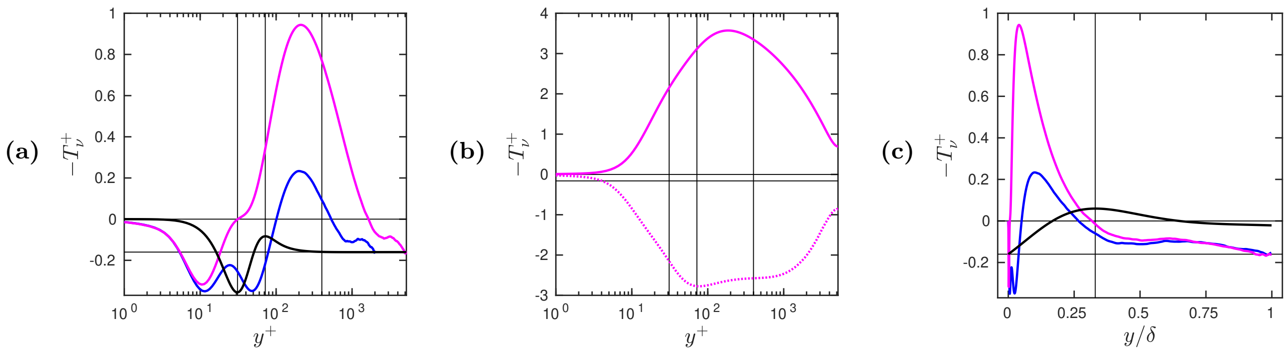

Fig. 11 : Evaluation of the model of Yoshizawa *et al.* (2012) in channel flow, using the DNS of Lee & Moser (2015). In **(a)**, the black curve shows $-D^+_{\nu ia}$ (19), the colored curves show $-T^+_{\nu Y}$ (31) for $Re_\tau = 1995$ (blue) and 5186 (magenta). In **(b)**, for $Re_\tau = 5186$, the curves show $\sigma_Y C_{\nu P}\ f_\nu\ k^+$ (continuous), $-\sigma_Y C_{\nu\epsilon}\ \frac{\epsilon^+}{k^+}\ \Lambda\ \nu^+$ (dotted). In **(a,b)** the vertical lines are at $y^+ = 31,\ 72$ and 400. In **(c)**, the black curve shows $-T^+_{\nu a}$ (24), the colored curves show $-T^+_{\nu Y}$ for $Re_\tau = 1995$ (blue) and 5186 (magenta), the vertical line is at $y = 0.33\delta$. In **(a,b,c)** the horizontal lines are at $-T_\nu^+ = 0$ and $-\kappa^2$.

not describe correctly the physics of the $\nu_t -$ equation in the near-wall region. It is also noticeable that no log-layer plateau appears in Spalart & Allmaras' model, even at $Re_\tau = 80000$, contrarily to what shows the exact $\nu_t -$ equation: compare the figures 6g and 10a. This raises question, since the classical 'log-layer equilibrium' has been used in the derivation of the model of Spalart & Allmaras (1994) to relate c_{w1} to the other coefficients.
Plots with y/δ as the abscissa are displayed on the figure 10c. The outer production peak of $-T^+_{\nu S}$, which was already visible for the lowest values of Re_τ in the figure 10a, seems, on the figure 10c, to scale with y/δ. Moreover, the value of this outer maximum has the correct magnitude. It is also remarkable that the values of $-T^+_{\nu S}$ at $y = \delta$ are quite correct. Thus, in the outer region there is a qualitative and even semi-quantitative agreement between the model of Spalart & Allmaras (1994) and the properties (T,P) of the exact $\nu_t -$ equation. However, the fact that the colored curves of the figure 10c differ significantly from the black curve, especially for the largest value of Re_τ , reveals that there are, in the outer region, quantitatively significant differences between the model and the exact theory.
In summary, the model of Spalart & Allmaras (1994) appears to be of poor quality in the inner region, and of rather good relevance in the outer region.

3.2 About the model of Yoshizawa *et al.* (2012)

The model of Yoshizawa *et al.* (2012) implies three turbulent fields: the eddy viscosity ν_t , the turbulent kinetic energy k and the turbulent dissipation ϵ. It also proposes an eddy-viscosity equation, which was shown to yield a better model of ν_t than the eddy-viscosity formula of the standard $k-\epsilon$ model in some specific cases. The high-Reynolds number form of the $\nu_t -$ equation (60) of Yoshizawa *et al.* (2012) reads, for channel flow,

$$\sigma_Y \frac{\partial \nu_t}{\partial t} \ = \ 0 \ = \ \frac{\partial}{\partial y}\Big(\nu_t \frac{\partial \nu_t}{\partial y}\Big) \ + \ \sigma_Y C_{\nu P}\ f_\nu\ k \ - \ \sigma_Y C_{\nu\epsilon}\ \frac{\nu_t}{\tau}\ , \tag{29}$$

with the same notations, except for σ_Y which stands for the σ_ν of Yoshizawa *et al.* (2012), and

$$f_\nu \ = \ \Big(1-\exp\Big(-\frac{y^*}{14}\Big)\Big)^2 \left(1+\frac{5}{R_t^{3/4}}\exp\left(-\Big(\frac{R_t}{200}\Big)^2\right)\right)\ ,\quad \tau \ = \ \frac{k}{\epsilon\ \Lambda}\ ,\quad \Lambda \ = \ \sqrt{1+2(C_S+C_\Omega)\Big(\frac{kS}{\epsilon}\Big)^2}\ , \tag{30}$$

$\sigma_Y = 3,\ \ C_{\nu P} = 4/15,\ \ C_{\nu\epsilon} = 3.5,\ \ C_S = 0.015,\ C_\Omega = 0.02C_S,\ \ y^* = (\nu\epsilon)^{1/4}\ y/\nu,\ R_t = k^2/(\nu\epsilon)$. Their model for $-T_\nu^+$ reads therefore

$$-\,T^+_{\nu Y} \ = \ \sigma_Y C_{\nu P}\ f_\nu\ k^+ \ - \ \sigma_Y C_{\nu\epsilon}\ \frac{\epsilon^+}{k^+}\ \Lambda\ \nu^+ \tag{31}$$

with, in particular,

$$k^+ \ = \ \frac{k}{u_\tau^2}\ ,\quad \epsilon^+ \ = \ \frac{\nu\epsilon}{u_\tau^4}\ ,\quad y^* \ = \ (\epsilon^+)^{1/4}\ y^+\ ,\quad R_t \ = \ \frac{k^{+2}}{\epsilon^+}\ ,\quad \frac{kS}{\epsilon} \ = \ \frac{k^+S^+}{\epsilon^+}\ . \tag{32}$$

Since the fields k and ϵ are needed in this model, we use the DNS data of Lee & Moser (2015) to test it. The reduced eddy viscosity ν^+ is also extracted from the DNS. Plots with y^+ as the abscissa are displayed on the figures 11ab. A good property of the model of Yoshizawa *et al.* (2012) is that it presents a dissipation peak in the near-wall region, that has the correct magnitude, and seems to scale with y^+. Thus the properties (D0,D1) of the theory are

qualitatively fulfilled. However, quantitatively, the dissipation peak of $-T^+_{\nu Y}$ comes in too early in terms of y^+ values: for $Re_\tau = 5186$, $-T^+_{\nu Y}$ shows a minimum around $y^+ = 10$ instead of $y^+ = 31$ for the minimum of $-D^+_{\nu ia}$. For larger values of y^+, the model of Yoshizawa *et al.* (2012) appears to be too productive, and there is no log-layer plateau.
Plots with y/δ as the abscissa are displayed on the figure 11c. These plots confirm that the model of Yoshizawa *et al.* (2012) is too productive, moreover the scaling with y/δ does not show up, i.e., the properties (T,P) of the theory are not fulfilled.
In summary, the model of Yoshizawa *et al.* (2012) appears to be of rather good relevance in the near-wall region, but of poor quality in the outer region. Moreover, this model shows a too strong Reynolds-number dependence.

Importantly, the equation (60) of Yoshizawa *et al.* (2012) contains a low-Reynolds number term, the viscous diffusion term

$$V_\nu \;=\; \frac{\partial}{\partial y}\Big(\nu\frac{\partial \nu_t}{\partial y}\Big)\;. \tag{33}$$

A quantitative study of this term, for channel flow, is proposed in our appendix C. It is shown that, for $y^+ \geq 1$ and $Re_\tau = 1995$ or 5186, $|V^+_\nu| \leq 0.023$. This is quite smaller than the turbulent dissipation peak, $\max D^+_{\nu ia} \simeq 0.36$, which gives the order of magnitude of the transport term, see the properties (D0,D1). Thus, taking into account this term, by adding $\sigma_Y V_\nu$ to the rhs of the equation (29), would modify only slightly the colored curves of the figures 11, and the discrepancies with the exact model would not disappear.

3.3 About the SAS models of Menter et al.

3.3.1 Basic model

The high-Reynolds number $k - \sqrt{k}\ell$ SAS model of Menter et al. has been introduced in Menter *et al.* (2006); Menter & Egorov (2010). The two turbulent fields are k and $\sqrt{k}\ell$ with ℓ the turbulent length scale. The product $\sqrt{k}\ell$ is up to a constant factor the eddy viscosity ν_t , hence this model may be presented as a $k - \nu_t$ model. After multiplication by $\rho^{-1}\, c_\mu^{1/4}\, \sigma_M$, with the notations of Menter *et al.* (2006), except for σ_M which stands for their σ_Φ , their equation (7) reads, for channel flow,

$$\sigma_M\frac{\partial \nu_t}{\partial t} \;=\; 0 \;=\; \frac{\partial}{\partial y}\Big(\nu_t\frac{\partial \nu_t}{\partial y}\Big) \;+\; P_{\nu M}\left(\zeta_1 - \zeta_2\Big(\frac{\ell}{\ell_{vK}}\Big)^2\right) \;-\; \sigma_M c_\mu^{1/4}\zeta_3\; k \tag{34}$$

$$\text{with}\quad P_{\nu M} \;=\; \sigma_M\frac{\nu_t^2 S^2}{k}\;,\quad \ell \;=\; c_\mu^{-1/4}\,\frac{\nu_t}{\sqrt{k}}\;,\quad \ell_{vK} \;=\; \kappa_M\left|\frac{S}{\partial S/\partial y}\right|\;, \tag{35}$$

$\sigma_M = 2/3,\ c_\mu = 0.09,\ \kappa_M = 0.41,\ \zeta_1 = 0.8,\ \zeta_2 = \zeta_1 - \zeta_3/c_\mu^{3/4} + \kappa_M^2/(\sigma_M c_\mu^{1/2}) = 1.47,\ \zeta_3 = 0.0288$. The definition of the von Karman length scale in (35) agrees perfectly with our definition (15), except for the different value of the von Karman constant; for the sake of brevity we use the same notation ℓ_{vK} , whereas in this section κ_M is used instead of κ for the computation of the SAS term, proportional to $(\ell/\ell_{vK})^2$, in (34). Menter's SAS model for $-T^+_\nu$ reads therefore

$$-\,T^+_{\nu M} \;=\; P^+_{\nu M}\left(\zeta_1 - \zeta_2\Big(\frac{\ell^+}{\ell^+_{vK}}\Big)^2\right) \;-\; \sigma_M c_\mu^{1/4}\zeta_3\; k^+ \tag{36}$$

$$\text{with}\quad P^+_{\nu M} \;=\; \sigma_M\frac{\nu^{+2} S^{+2}}{k^+}\;,\quad \ell^+ \;=\; c_\mu^{-1/4}\,\frac{\nu^+}{\sqrt{k^+}}\;. \tag{37}$$

The DNS data of Lee & Moser (2015) are used to test this model. Finite differences are used to compute $\partial S^+/\partial y^+$ to estimate ℓ^+_{vK} . Plots with y^+ as the abscissa are displayed on the figures 12ab. The figure 12a shows that there is a near-wall dissipation peak in the SAS model, at a fixed y^+ position, i.e. the properties (D0,D1) of the theory are qualitatively fulfilled. However, the minimum value of $-T^+_{\nu M}$ corresponding to this dissipation peak is too small, and this peak comes in too late in terms of y^+ values: for $Re_\tau = 5186$, $-T^+_{\nu M}$ shows a minimum around $y^+ = 43$ instead of $y^+ = 31$ for the minimum of $-D^+_{\nu ia}$. For larger values of y^+, no log-layer plateau shows up in the SAS profiles, at least for $Re_\tau \lesssim 5200$, whereas the classical 'log-layer equilibrium' has been used in the derivation of the model of Menter *et al.* (2006) to relate ζ_2 to the other coefficients. The figure 12b showing the different contributions to $-T^+_{\nu M}$ proves that the SAS term in (36) plays a quite important role, both around $y^+ = 43$ where $-T^+_{\nu M}$ has a negative peak, and near the centerplane, at $y^+ = \delta^+$, where it imposes a rather large negative value.
Plots with y/δ as the abscissa are displayed on the figure 12c. They show that $-T^+_{\nu M}$ scales with y/δ in the outer region, with a production peak around $y = 0.42\delta$, and then a decrease towards a negative value at the centerplane. Thus the properties (T,P) of the theory are qualitatively fulfilled.
In summary, of the three models tested up to now, the basic SAS model shows the best qualitative agreement with

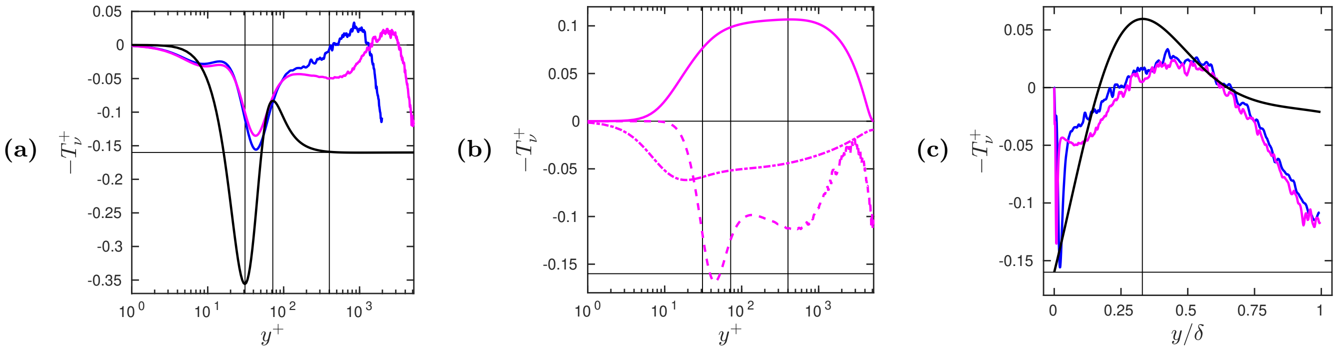

Fig. 12 : Evaluation of the SAS model of Menter *et al.* (2006) in channel flow, using the DNS of Lee & Moser (2015). In **(a)**, the black curve shows $-D^+_{\nu ia}$ (19), the colored curves show $-T^+_{\nu M}$ (36) for $Re_\tau = 1995$ (blue) and 5186 (magenta). In **(b)**, for $Re_\tau = 5186$, the curves show $\zeta_1\ P^+_{\nu M}$ (continuous), $-\zeta_2\ P^+_{\nu M}\ (\ell/\ell_{vK})^2$ (dashed), $-\sigma_M c_\mu^{1/4}\zeta_3\ k^+$ (dash-dot). In **(a,b)** the vertical lines are at $y^+ = 31,\ 72$ and 400. In **(c)**, the black curve shows $-T^+_{\nu a}$ (24), the colored curves show $-T^+_{\nu M}$ for $Re_\tau = 1995$ (blue) and 5186 (magenta), the vertical line is at $y = 0.33\delta$. In **(a,b,c)** the horizontal lines are at $-T^+_\nu = 0$ and $-\kappa^2$.

the theory. It also agrees semi-quantitatively with the theory, as shows the comparison between the figures 10c, 11c and 12c: only the latest shows model curves (the coloured curves) that live in the interval of values of the ordinate swept by the exact asymptotic profile (the black curve).

3.3.2 Study of the length scales and of the model with length scale limiters

In order to better analyze the SAS models, the figures 13abc display the two length scales implied and their ratio. The figures 13ab suggest that both length scales, scaled by δ, scale with y/δ, except in a narrow near-wall region for ℓ_{vK} . Since ℓ_{vK}/δ is computed from the DNS as

$$\frac{\ell^+_{vK}}{\delta^+} \ = \ \frac{\kappa_M}{\delta^+}\left|\frac{S^+}{\partial S^+/\partial y^+}\right| , \tag{38}$$

because both S^+ and $\partial S^+/\partial y^+$ become quite small in the outer region for large Re_τ , the DNS noise is amplified there. This explains the oscillations in the figures 13bc, that also blur some profiles in the figures 12. Smoother profiles of ℓ_{vK} may be obtained from the exact model of Heinz (2018, 2019) and have been shown on the figure 3. The laws that result from the log-layer theory,

$$\ell \ = \ \ell_{vK} \ = \ \kappa_M y \ , \tag{39}$$

are relevant in a narrow near-wall region for ℓ and in a larger region for ℓ_{vK} , which otherwise vanishes at the centerplane as already discussed after equation (15). The ratio ℓ/ℓ_{vK} displayed on the figure 13c shows consequently a near-wall peak of maximum value of order 1, which locates somehow the log-layer region. It then decays, since ℓ_{vK} increases first faster than ℓ, and finally increases again and diverges as $y \to \delta$. Obviously, the infinite value of ℓ/ℓ_{vK} at the centerplane plays a role in the too large value of $-T^+_{\nu M}$ in this region, see the figures 12bc.

From these observations, it seems relevant to test also the SAS model with length scale limiters, since these limiters have been defined 'in order of avoiding overly large or small values of the length scale ratio' ℓ/ℓ_{vK} , as explained by Menter *et al.* (2006) at the level of their equation (12). These length scale limiters are defined by

$$\ell/c_{\ell 1} \ < \ \ell_{vK} \ < \ c_{\ell 2}\ \kappa_M\ y \tag{40}$$

with $c_{\ell 1} = 10,\ c_{\ell 2} = 1.3$. The minimum and maximum limiters are displayed on the figures 13de for the highest Reynolds number available in the DNS database of Lee & Moser (2015). The maximum limiter is active in a narrow near-wall region, for $y^+ \lesssim 8$. There ℓ is quite small, hence ℓ/ℓ_{vK} remains small and is unchanged at the scales of the figures 13cf. The minimum limiter is active in a narrow region near the centerplane. As displayed on the figure 13f, the length scale ratio is mainly affected in this outer region, where it saturates to $\ell/\ell_{vK} = c_{\ell 1}$. This saturates the minimum peak of $-T^+_{\nu M}$ at the centerplane only marginaly, with reference to the figures 12bc. From this point of view, a lower value of $c_{\ell 1}$ would help.

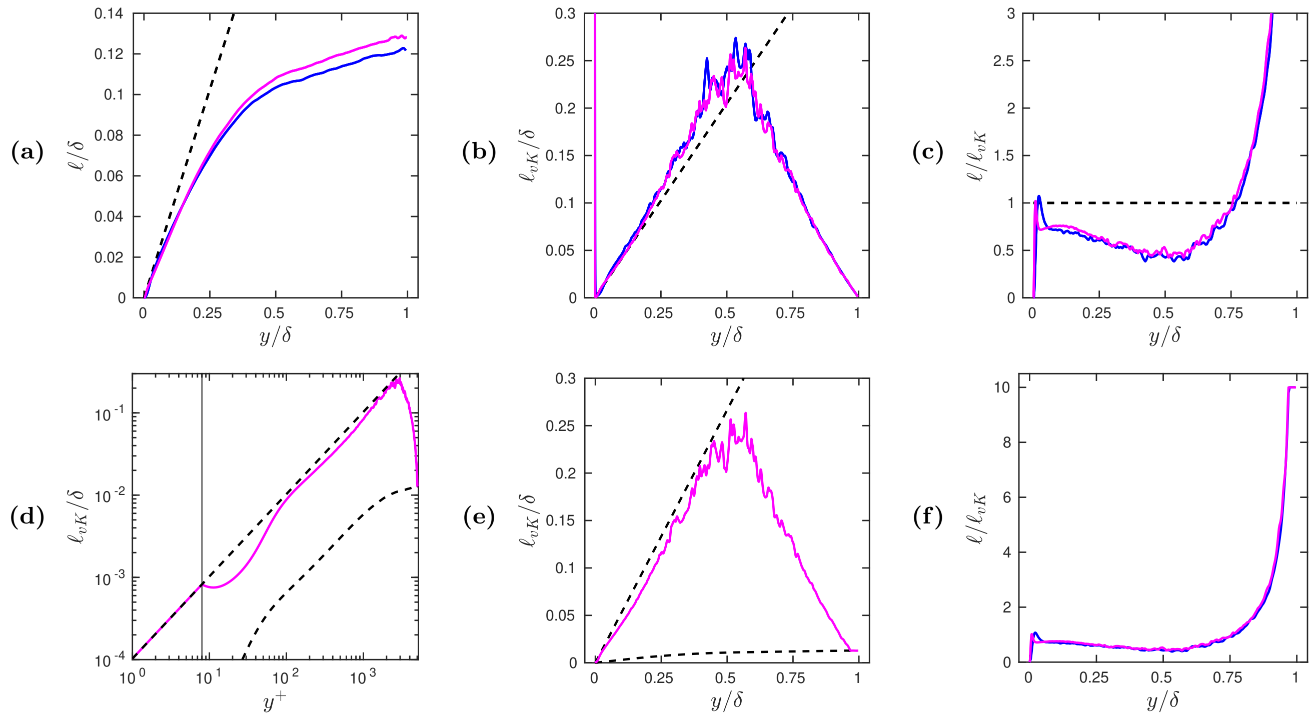

Fig. 13 : For channel flow, using the DNS of Lee & Moser (2015) at $Re_\tau = 1995$ (blue) and 5186 (magenta), the turbulent length scale ℓ **(a)**, the von Karman length scale ℓ_{vK} **(b)**, their ratio **(c)**. In **(a,b)** the dashed line shows the log-layer length scale $\kappa_M y^+$. The effects of the length scale limiters (40) is shown on **(d,e)** for $Re_\tau = 5186$, with the limiters shown by the dashed curves, and on **(f)** for both Reynolds numbers.

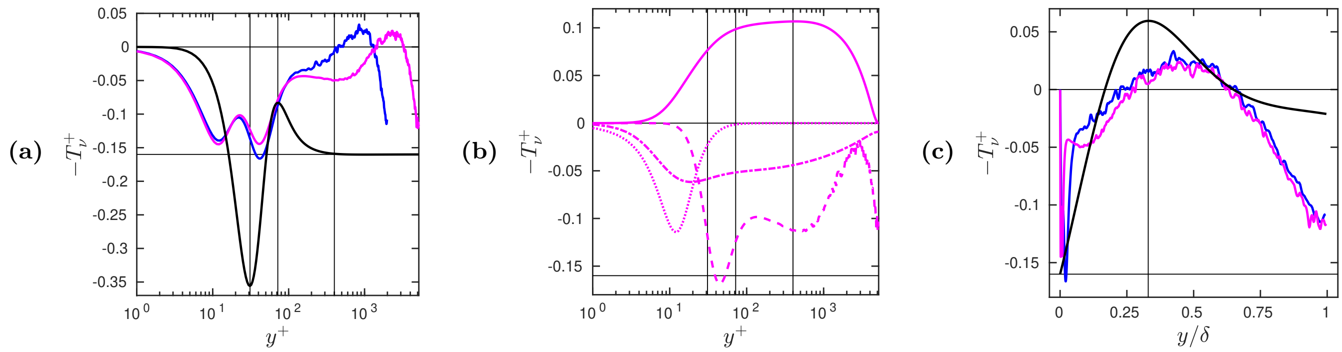

Fig. 14 : Same as the figures 12, but adding the viscous sublayer term VSM_ν^+ (43) to $-T_{\nu M}^+$ (36); VSM_ν^+ is shown with the dotted curve in **(b)**.

3.3.3 Model with a viscous sublayer term

In order to have a model valid through the viscous sublayer, Menter *et al.* (2006) add a viscous sublayer term to the r.h.s. of their ν_t - equation (34),

$$VSM_\nu \;=\; -\,6\sigma_M\; f_\Phi\; \frac{\nu\nu_t}{y^2}\;. \tag{41}$$

The dimensional factor in this term, $\nu\nu_t/y^2$, has similarities with the one of the last term of the ν_t - equation (25) of Spalart & Allmaras (1994), ν_t^2/y^2, with, however, one eddy viscosity replaced by the fluid viscosity. In (41),

$$f_\Phi \;=\; \frac{1+c_{d1}\xi}{1+\xi^4}\;,\quad \xi \;=\; \frac{\sqrt{0.3\;k}\;y}{20\nu}\;,\quad c_{d1} = 4.7\;. \tag{42}$$

In inner units,

$$VSM_\nu^+ \;=\; -\,6\sigma_M\; f_\Phi\; \frac{\nu^+}{y^{+2}} \quad \text{with} \quad \xi \;=\; \frac{\sqrt{0.3\;k^+}\;y^+}{20} \tag{43}$$

in the damping function f_Φ . The figures 14 show that the addition of VSM_ν^+ to $-T_{\nu M}^+$ introduce a new near-wall minimum peak in $-T_{\nu M}^+$, which does not really help since it occurs at too low values of y^+, and is too weak.

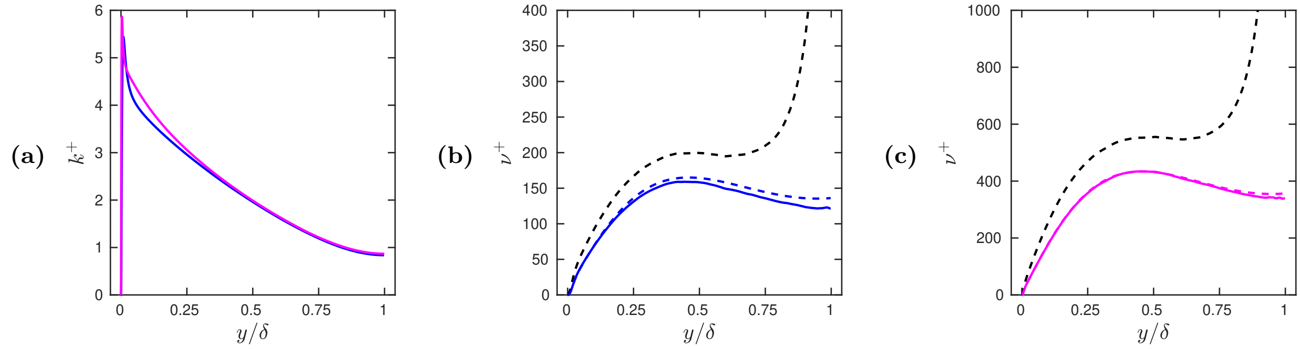

Fig. 15 : **(a)** The turbulent kinetic energy k^+ for the channel flow DNS of Lee & Moser (2015) at $Re_\tau = 1995$ (blue) and 5186 (magenta). **(b,c)** For $Re_\tau = 1995$ **(b)** or 5186 **(c)** the continuous colored curve shows ν^+ computed from the DNS, the continuous dashed curve ν^+ (5), the black dashed curve ν_m^+ (44).

3.3.4 Model with ν_t limiter

For the sake of completeness, we check that the ν_t limiter introduced in Menter *et al.* (2006) to deal with adverse pressure gradients or stagnation regions is inactive in channel flow. The equations (11) of Menter *et al.* (2006) state that the reduced eddy viscosity ν^+ should be smaller than

$$\nu_m^+ \;=\; \frac{a_1 k^+}{S^+} \quad \text{with} \quad a_1 = a_1^{SST} f_b + (1-f_b) a_1^{REAL} \;, \quad f_b = \tanh\left[\left(\frac{20(\nu^+ + 1)}{\kappa_M S^+ y^{+2} + 0.01}\right)^2\right] \;, \tag{44}$$

$a_1^{SST} = 0.32$, $a_1^{REAL} = 0.577$. Because the turbulent kinetic energy k^+ reaches rather large levels in the near-wall region, and then does not decrease too much outside, as shown on the figure 15a, whereas the mean strain rate S^+ decreases fast from 1 to 0 as y increases from 0 to δ, ν_m^+ is everywhere larger than ν^+, as shown on the figures 15bc.

4 A modified SAS model

In channel flow, the comparison of the figures 6 and 12 suggests that the SAS dissipation term $-\zeta_2 P_{\nu M} (\ell/\ell_{vK})^2$ of equation (34) may be responsible of the main discrepancies between the exact and SAS models. We therefore propose a modified SAS model where the terms proportional to ζ_1 and ζ_3 in equation (34) are kept, whereas the SAS dissipation term is replaced by a term similar to $D_{\nu i}$ (13a),

$$D_{\nu N} \;=\; \kappa^2 \, \frac{\nu_t^2}{\ell_{vK}^2} \, \frac{1}{f^2} \;. \tag{45}$$

Our modified SAS ν_t - equation thus reads, in turbulent wall flows,

$$\sigma_M \frac{\partial \nu_t}{\partial t} \;=\; 0 \;=\; \frac{\partial}{\partial y}\left(\nu_t \frac{\partial \nu_t}{\partial y}\right) \;+\; \zeta_1 P_{\nu M} \;-\; D_{\nu N} \;-\; \sigma_M c_\mu^{1/4} \zeta_3 \, k \;. \tag{46}$$

The replacement of L_{vK} in $D_{\nu i}$ by ℓ_{vK} in $D_{\nu N}$ is important to insure that this modified model may be as 'sensitive' as the original SAS model: both the original dissipation term $-\zeta_2 P_{\nu M} (\ell/\ell_{vK})^2$ and the modified dissipation term $-D_{\nu N}$ are proportional to ℓ_{vK}^{-2} . To obtain a correct behaviour of $D_{\nu N}$ in the near-wall region, that is, a behaviour similar to that of $D_{\nu i}$, it is important to not use a maximum limiter of ℓ_{vK} proportional to y, as Menter et al. did it, see (40). This would impose $\ell_{vK} = 0$ at the wall, which is according to us not physical. Therefore, we use only a minimum limiter on ℓ_{vK} ,

$$\ell / c_{\ell 1} \;<\; \ell_{vK} \;, \tag{47}$$

with a lower value of $c_{\ell 1} = 1$ to saturate $D_{\nu N}$ near the centerplane. With the same coefficients ζ_1 , ζ_3 as the ones chosen by Menter et al., a test of this modified model, which leads to

$$-\,T_{\nu N}^+ \;=\; \zeta_1 P_{\nu M}^+ \;-\; D_{\nu N}^+ \;-\; \sigma_M c_\mu^{1/4} \zeta_3 \, k^+ \tag{48}$$

$$\text{with} \quad D_{\nu N}^+ \;=\; \kappa^2 \, \frac{\nu^{+2}}{\ell_{vK}^{+2}} \, \frac{1}{f^2} \;, \tag{49}$$

is proposed on the figures 16. The comparison with the figures 12 proves that a much better agreement with the exact model is reached. More precisely, the curves of the figure 16a are quite similar to the corresponding ones of the

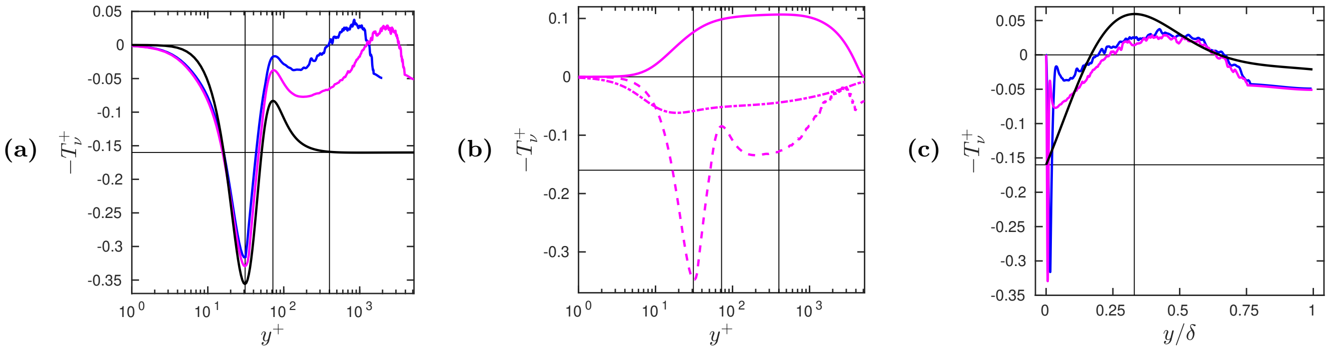

Fig. 16 : Evaluation of the modified SAS model (46) in channel flow, using the DNS of Lee & Moser (2015). In **(a)**, the black curve shows $-D_{\nu ia}^+$ (19), the colored curves show $-T_{\nu N}^+$ (48) for $Re_\tau = 1995$ (blue) and 5186 (magenta). In **(b)**, for $Re_\tau = 5186$, the curves show $\zeta_1\ P_{\nu M}^+$ (continuous), $-D_{\nu N}^+$ (dashed), $-\sigma_M c_\mu^{1/4}\zeta_3\ k^+$ (dash-dot). In **(a,b)** the vertical lines are at $y^+ = 31,\ 72$ and 400. In **(c)**, the black curve shows $-T_{\nu a}^+$ (24), the colored curves show $-T_{\nu M}^+$ for $Re_\tau = 1995$ (blue) and 5186 (magenta), the vertical line is at $y = 0.33\delta$. In **(a,b,c)** the horizontal lines are at $-T_\nu^+ = 0$ and $-\kappa^2$.

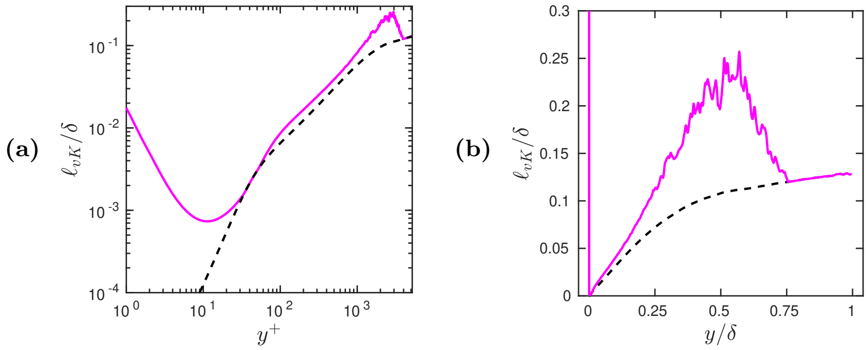

Fig. 17 : Characterization of the modified SAS model (46) regarding length scales, for channel flow, using the DNS of Lee & Moser (2015) at $Re_\tau = 5186$. The magenta curves show the limited von Karman length scale ℓ_{vK} and the black curves its limiter, i.e., the turbulent length scale ℓ.

figure 6g, whereas the ones of the figure 16c are very similar to the corresponding ones of the figure 6h: now all the properties (D,T,P) of the exact model, listed in the section 2.10, are quantitatively recovered.
To complete the presentation of this modified model, the von Karman length scale and its minimum limiter, i.e., the turbulent length scale, are plotted on the figures 17, which should be compared to the figures 13de. Note that $\kappa = 0.40$ has been used in this section, instead of $\kappa_M = 0.41$ in the previous one.

5 Concluding discussion

The recent availability of the large DNS and experimental databases of Lee & Moser (2015) in channel flows, Chin *et al.* (2014) in pipe flows, Sillero *et al.* (2013); Vallikivi *et al.* (2015) in boundary layers, that span wide intervals of values of Reynolds numbers, has allowed the development of the analytic RANS theory of Heinz (2018, 2019) for these 'turbulent wall flows'. This theory, which offers the analytic formula (5) for the eddy viscosity ν_t , has been used here as a starting point to propose an order 2 transport equation (11) for ν_t , based on the idea that it contains a standard transport term T_ν balanced by production and dissipation terms, P_ν and D_ν , in steady mean flows: for such flows the eddy viscosity budget reads simply $T_\nu + P_\nu - D_\nu = 0$. These terms are known analytically, at finite and infinite Re_τ , either in the inner, log layer or outer regions for the latter case, as summarized on the table 1. To our knowledge, this is the first time that a systematic budget for the eddy viscosity is presented at finite and infinite Reynolds numbers, and the first time that a budget of a turbulent quantity at infinite Reynolds number is presented. All this offers an understanding of the mechanisms at play, as summarized in our section 2.10, which also shows that our ν_t budget and the known k budget (at finite Reynolds number only) differ quite much. In the ν_t budget, noticeable is the fact that dissipation dominates in the inner region, and takes the same universal form $D_{\nu i}$ (13a) for all turbulent wall flows. This form identifies as the relevant length scale the universal asymptotic von Karman length scale L_{vK} (14) and a universal damping function f (16). All this has been used as a test bench of existing models that present a ν_t - equation with the same transport term. Thus, we have evidenced some deficiencies of the models of Spalart & Allmaras (1994); Yoshizawa *et al.* (2012), which were designed before the publication of the databases mentioned hereabove. The SAS models of Menter *et al.* (2006); Menter & Egorov (2010) have also been studied, and have given better results. Finally, quantitative discrepancies between the SAS ν_t - budget and our exact ν_t - budget have been resolved by a modification of the SAS dissipation term in the ν_t - equation. We suggest to use the form of the exact $D_{\nu i}$ (13a), but replacing the universal asymptotic von Karman length scale L_{vK} by the local von Karman length scale ℓ_{vK} (15), limited from below by the turbulent length scale ℓ. This limited von Karman length scale shows, at least in channel flow, a profile similar to the one of L_{vK} : compare the figures 3ab and 17ab. The fact that the limited von Karman length scale is flow-dependent and appears at the power -2 in the dissipation term suggests that the modified model could be, in unsteady simulations of complex flows, as 'sensitive' or 'scale-adaptive' as the models of Menter *et al.* (2006); Menter & Egorov (2010), but with a better behaviour in the near-wall region.

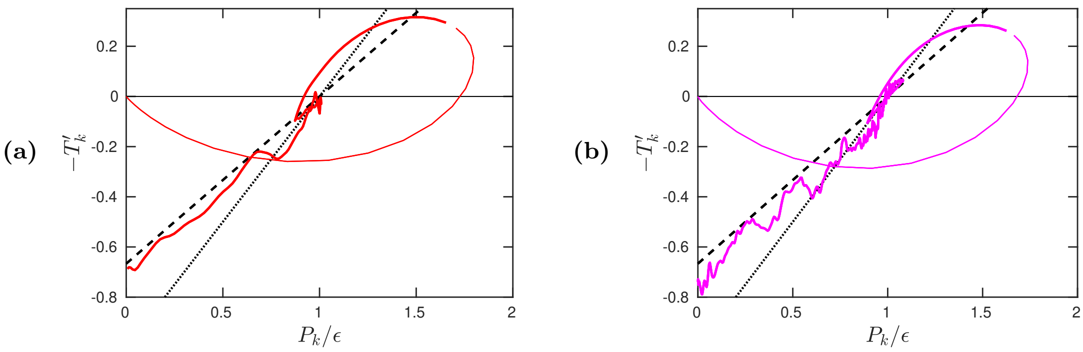

Fig. A.1 : The continuous curve shows the opposite of the normalized transport term $-T'_k$ (A.2) vs the production-to-dissipation ratio P_k/ϵ for the channel flow DNS of Lee & Moser (2015) at $Re_\tau = 543$ **(a)**, 5186 **(b)**. The thin (resp. thick) curve corresponds to the inner region $y^+ < 15$ (resp. outer region $y^+ > 15$). The dashed (resp. dotted) line shows the model (A.3) with $\sigma_k = 2/3$ (resp. 1).

Appendices

A Validation of the standard k - equation with channel flow DNS

In the standard, high-Reynolds number $k - \epsilon$ (Launder & Spalding 1974) and $k - \omega$ (Wilcox 1988) models, for channel flows, the closed k - equation reads

$$\sigma_k \frac{\partial k}{\partial t} \; = \; 0 \; = \; \frac{\partial}{\partial y}\Big(\nu_t \; \frac{\partial k}{\partial y}\Big) \; + \; \sigma_k \; (P_k \; - \; \epsilon) \tag{A.1}$$

with σ_k a model coefficient, and the production term

$$P_k \; = \; \nu_t \; S^2$$

according to the eddy-viscosity hypothesis, with the notations of section 2.1. The equation (A.1) is also used in the SAS model of Menter *et al.* (2006); Menter & Egorov (2010). Various values of σ_k are recommended: $\sigma_k = 1$ in Launder & Spalding (1974), 2 in Wilcox (1988), 2/3 in Menter *et al.* (2006). To discriminate between those, and confirm the relevance of the k - equation, we analyze the equation (A.1) with the approach of Heinz (2006). After division by ϵ, equation (A.1) states that the opposite of the dimensionless normalized transport term

$$-\,T'_k \; = \; -\,\frac{1}{\epsilon}\,\frac{\partial}{\partial y}\Big(\nu_t \; \frac{\partial k}{\partial y}\Big) \tag{A.2}$$

should be a linear function of the production-to-dissipation ratio P_k/ϵ,

$$-\,T'_k \; = \; \sigma_k \; (P_k/\epsilon \; - \; 1) \; . \tag{A.3}$$

This prediction is tested on the channel flow DNS data of Lee & Moser (2015) on the figures A.1. Note that Lee & Moser (2015) offer in their figure 7 plots of P_k/ϵ vs y^+. The eddy viscosity ν_t is computed according to its definition (3), and the derivatives by y in T'_k are computed by finite differences. The figures A.1 show that, in the outer region $y^+ > 15$, the DNS curves remain close to the line (A.3): this confirms the relevance of the high-Reynolds number k - equation (A.1), and supports Menter *et al.* (2006) in their choice $\sigma_k = 2/3$. The value of Launder & Spalding (1974), $\sigma_k = 1$, seems a bit too large, whereas the value of Wilcox (1988), $\sigma_k = 2$, seems clearly too large.

B Study of the standard ϵ and ω - equations with channel flow DNS

By analogy with (A.1), Launder & Spalding (1974) postulated in the $k - \epsilon$ model the ϵ - equation, for channel flows,

$$\sigma_\epsilon \frac{\partial \epsilon}{\partial t} \; = \; 0 \; = \; \frac{\partial}{\partial y}\Big(\nu_t \; \frac{\partial \epsilon}{\partial y}\Big) \; + \; \sigma_\epsilon \frac{\epsilon}{k} \; (C_1 P_k \; - \; C_2 \epsilon) \tag{B.1}$$

with $\sigma_\epsilon = 1.3,\; C_1 = 1.44,\; C_2 = 1.92$. After division by ϵ^2/k, equation (B.1) states that the opposite of the normalized transport term

$$-\,T'_\epsilon \; = \; -\,\frac{k}{\epsilon^2}\,\frac{\partial}{\partial y}\Big(\nu_t \; \frac{\partial \epsilon}{\partial y}\Big) \tag{B.2}$$

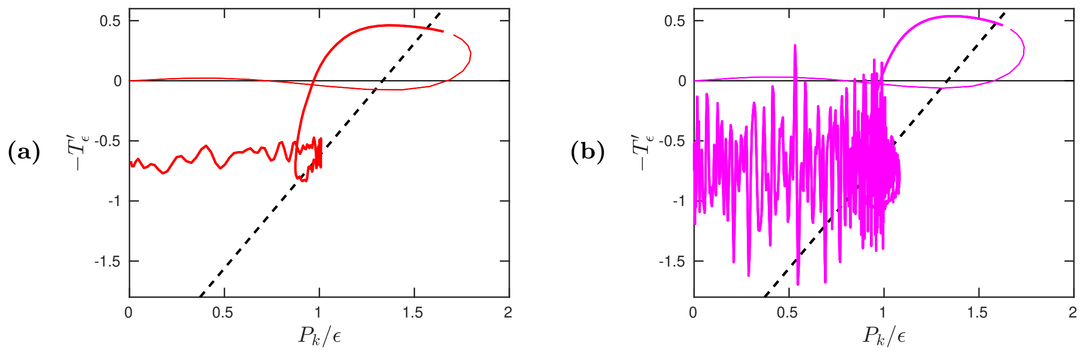

Fig. B.1 : The continuous curve shows the opposite of the normalized transport term $-T'_\epsilon$ (B.2) for the channel flow DNS of Lee & Moser (2015) at $Re_\tau = 543$ **(a)**, 5186 **(b)**. The thin (resp. thick) curve corresponds to the inner region $y^+ < 15$ (resp. outer region $y^+ > 15$). The dashed line shows the standard model (B.3).

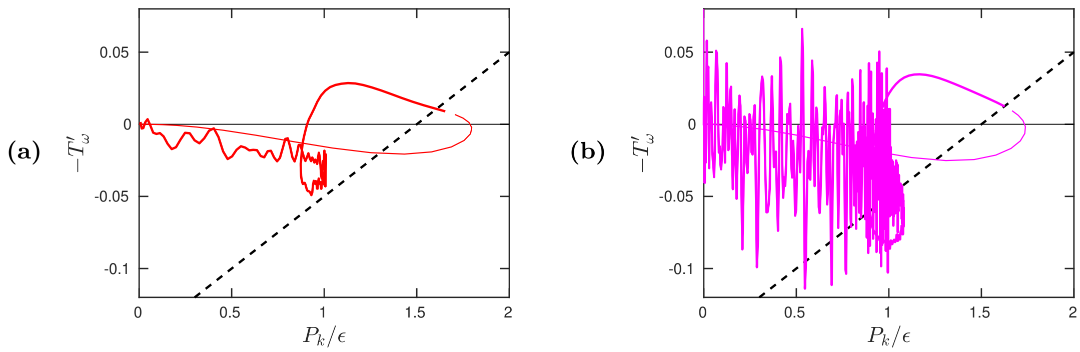

Fig. B.2 : The continuous curve shows the opposite of the normalized transport term $-T'_\omega$ (B.5) for the channel flow DNS of Lee & Moser (2015) at $Re_\tau = 543$ **(a)**, 5186 **(b)**. The thin (resp. thick) curve corresponds to the inner region $y^+ < 15$ (resp. outer region $y^+ > 15$). The dashed line shows the standard model (B.6).

should be a linear function of P_k/ϵ,

$$-T'_\epsilon \;=\; \sigma_\epsilon\,(C_1 P_k/\epsilon \;-\; C_2)\;. \tag{B.3}$$

This prediction is tested on the channel flow DNS of Lee & Moser (2015) on the figures B.1. Since ϵ becomes quite small near the centerplane (see e.g. the figure 9 of Heinz 2019), there the DNS noise is amplified: this region corresponds to the lower intersection of the curves of the figures B.1 with the axis $P_k/\epsilon = 0$ i.e. $P_k = 0$ (see the figure 7 of Lee & Moser 2015). The figures B.1, to be compared with the figures A.1, show DNS curves that do not align with the linear model (B.3), even if one considers only their outer-region part. The structure of the curves is highly nonlinear, therefore a change of the model constants σ_ϵ , C_1 and C_2 cannot solve this problem.

A similar flaw exists with the ω - equation of the standard $k-\omega$ model of Wilcox (1988). With a slight change of notation, to introduce a coefficient σ_ω that plays a role similar to the coefficients σ_k in (A.1) and σ_ϵ in (B.1), Wilcox' equation for

$$\omega \;=\; \epsilon/(\beta^* k)$$

reads, for channel flows,

$$\sigma_\omega \frac{\partial \omega}{\partial t} \;=\; 0 \;=\; \frac{\partial}{\partial y}\Big(\nu_t\,\frac{\partial \omega}{\partial y}\Big) \;+\; \sigma_\omega \frac{\omega}{k}\,\Big(\gamma P_k \;-\; \frac{\beta}{\beta^*}\epsilon\Big) \tag{B.4}$$

where $\sigma_\omega = 2,\ \gamma = 5/9,\ \beta = 3/40,\ \beta^* = 9/100$. After division by ω^2, equation (B.4) states that

$$-T'_\omega \;=\; -\frac{1}{\omega^2}\frac{\partial}{\partial y}\Big(\nu_t\,\frac{\partial \omega}{\partial y}\Big) \tag{B.5}$$

should be a linear function of P_k/ϵ,

$$-T'_\omega \;=\; \sigma_\omega\,(\beta^*\gamma P_k/\epsilon \;-\; \beta)\;. \tag{B.6}$$

The figures B.2 show again a highly nonlinear structure of the channel flow DNS curves, that cannot fit a linear model such as (B.6), even in the outer region $y^+ > 15$.

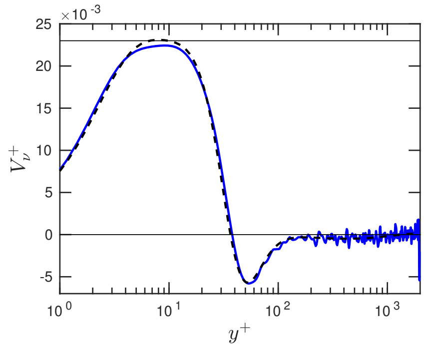

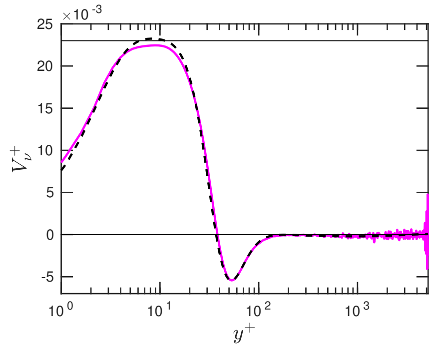

Fig. C.1 : The continuous curve shows the dimensionless viscous diffusion term V_ν^+ (C.1) for the channel flow DNS of Lee & Moser (2015) at $Re_\tau = 1995$ (**a**), 5186 (**b**). The dashed curve shows the analytical model that can be derived from (5). The horizontal lines are at $V_\nu^+ = 0$ and 0.023.

C Study of the viscous diffusion term in the ν_t - equation

The viscous diffusion term V_ν defined in the equation (33) reads, in dimensionless form,

$$V_\nu^+ \;=\; \frac{V_\nu}{u_\tau^2} \;=\; \frac{\partial^2 \nu^+}{\partial y^{+2}} \;. \tag{C.1}$$

It can be computed numerically with finite differences from channel flow DNS data. It can also be computed analytically starting from (5). A comparison of both estimates of V_ν^+, for relevant cases (the ones also studied in section 3.2), is displayed on the figures C.1. The analytic model is overall quite good. Moreover, everywhere, $|V_\nu^+| \leq 0.023$.

References

ABDOL-HAMID, K. S. 2015 Assessments of $k-kL$ Turbulence Model Based on Menter's Modification to Rotta's Two-Equation Model. *Int. J. Aerospace Engineering* **2015**, 1–18, http://downloads.hindawi.com/journals/ijae/2015/987682.pdf.

BALDWIN, B. & BARTH, T. 1990 A one-equation turbulence transport model for high Reynolds number wall-bounded flows. *NASA Technical Memorandum* pp. 102847, 1–20.

CHIN, C., MONTY, J. & OOI, A. 2014 Reynolds number effects in DNS of pipe flow and comparison with channels and boundary layers. *Int. J. Heat & Fluid Flow* **45**, 33 – 40.

EGOROV, Y., MENTER, F., LECHNER, R. & COKLJAT, D. 2010 The scale-adaptive simulation method for unsteady turbulent flow predictions. Part 2: Application to complex flows. *Flow, Turbulence & Comb.* **85**, 139–165.

HAMBA, F. 2005 Nonlocal analysis of the Reynolds stress in turbulent shear flow. *Phys. Fluids* **17**, 115102.

HAMBA, F. 2013 Exact transport equation for local eddy viscosity in turbulent shear flow. *Phys. Fluids* **25**, 085102.

HANJALIĆ, K. & LAUNDER, B. 2011 *Modelling turbulence in engineering and the environment: second-moment routes to closure*. Cambridge University Press.

HEINZ, S. 2006 Turbulent supersonic channel flow: direct numerical simulation and modeling. *AIAA Journal* **44**, 3040–3050.

HEINZ, S. 2018 On mean flow universality of turbulent wall flows. I. High Reynolds number flow analysis. *J. Turbulence* **19**, 929–958.

HEINZ, S. 2019 On mean flow universality of turbulent wall flows. II. Asymptotic flow analysis. *J. Turbulence* **20**, 174–193.

HOYAS, S. & JIMÉNEZ, J. 2008 Reynolds number effects on the Reynolds-stress budgets in turbulent channels. *Phys. Fluids* **20**, 101511, 1–8.

JAKIRLIC, S. & MADUTA, R. 2015 Extending the bounds of steady RANS closures: Toward an instability-sensitive Reynolds stress model. *Int. J. of Heat & Fluid Flow* **51**, 175–194.

KOLMOGOROV, A. N. 1942 Equations of turbulent motion in an incompressible fluid. *Selected works of A. N. Kolmogorov*, pp. 328–330. Springer 1991, ed. V. M. Tikhomirov, translated from the Russian by V. M. Volosov.

LAUNDER, B. E. & SPALDING, D. B. 1974 The numerical computation of turbulent flows. *Comp. Meth. Appl. Mech. Eng.* **3**, 269–289.

LEE, M. & MOSER, R. D. 2015 Direct numerical simulation of turbulent channel flow up to $Re_\tau \approx 5200$. *J. Fluid Mech.* **774**, 395–415.

MENTER, F. R. & EGOROV, Y. 2010 The scale-adaptive simulation method for unsteady turbulent flow predictions. Part 1: theory and model description. *Flow, Turbulence & Comb.* **85**, 113–138.

MENTER, F. R., EGOROV, Y. & RUSCH, D. 2006 Steady and unsteady flow modelling using the $k-\sqrt{k}L$ model. *Ichmt Digital Library Online*. Begell House Inc.

NEE, V. W. & KOVASZNAY, L. S. G. 1969 Simple phenomenological theory of turbulent shear flows. *Phys. Fluids* **12**, 473–484.

SILLERO, J. A., JIMÉNEZ, J. & MOSER, R. D. 2013 One-point statistics for turbulent wall-bounded flows at Reynolds numbers up to $\delta^+ \simeq 2000$. *Phys. Fluids* **25**, 105102,1–16.

SPALART, P. & ALLMARAS, S. 1994 A one-equation turbulence model for aerodynamic flows. *Recherche Aérospatiale* **1**, 5–21.

VALLIKIVI, M., HULTMARK, M. & SMITS, A. J. 2015 Turbulent boundary layer statistics at very high Reynolds number. *J. Fluid Mech.* **779**, 371–389.

WILCOX, D. C. 1988 Reassessment of the scale-determining equation for advanced turbulence models. *AIAA Journal* **26**, 1299–1310.

WILCOX, D. C. 2006 *Turbulence Modeling for CFD*. DCW Industries.

YOSHIZAWA, A., ABE, H., MATSUO, Y., FUJIWARA, H. & MIZOBUCHI, Y. 2012 A Reynolds-averaged turbulence modeling approach using three transport equations for the turbulent viscosity, kinetic energy, and dissipation rate. *Phys. Fluids* **24**, 075109.

Archives: links to important previous versions

- **V0.135 of August 26, 2020, quite similar to the V0.13 of July 17, 2020 read by Stefan:** memory of the **QR7,8 regarding variants of the SAS model**.
- **V0.11 of June 18, 2020:** memory of the **section 4.3 About the model of Hamba (2013)** with a study of its production term.
- **V0.085 of June 4, 2020:** memory of the **section 3.8 QR6 on the BL case inspired from Spalart & Allmaras (1994)** - possible advection effects that might change the lhs of the ν_t eq.
- **V0.055 of May 19, 2020:** memory of the **section 4.1 Comparison with Hamba (2013)**, of **figure 9** for P_ν and $P_{\nu H}$, of **QR5** regarding this comparison.
- **V0.025 of May 7, 2020:** memory of **figure 5** for W'/W and $(W'^2 + WW'')/W^2$, **QR3** regarding comparisons with DNS of pipe flow, **QR4** regarding comparisons with DNS of BL, **figure 10** for $-T_\nu^+$ et al. in BL with an extended range of y^+.
- **V0.015 of April 29, 2020:** memory of **QR1** regarding near-wall effects / the kinematic viscosity & **QR2** regarding pipe flow / curvature effects.